Long-term observations of cloud condensation nuclei in the Amazon rain forest – Part 2: Variability and characteristic differences under near-pristine, biomass burning, and long-range transport conditions

Mira L. Pöhlker[1], Florian Ditas[1], Jorge Saturno[1], Thomas Klimach[1], Isabella Hrabě de Angelis[1],
Alessandro Araùjo[2], Joel Brito[3a], Samara Carbone[3b], Yafang Cheng[1], Xuguang Chi[1c], Reiner Ditz[1],
Sachin S. Gunthe[4], Konrad Kandler[5], Jürgen Kesselmeier[1], Tobias Könemann[1], Jošt V. Lavrič[6],
Scot T. Martin[7,8], Eugene Mikhailov[9], Daniel Moran-Zuloaga[1], Luciana V. Rizzo[10], Diana Rose[11],
Hang Su[1], Ryan Thalman[12,d], David Walter[1], Jian Wang[12], Stefan Wolff[1], Henrique M. J. Barbosa[3],
Paulo Artaxo[2], Meinrat O. Andreae[1,13], Ulrich Pöschl[1] and Christopher Pöhlker[1]

[1] *Multiphase Chemistry and Biogeochemistry Departments, Max Planck Institute for Chemistry, 55020 Mainz, Germany.*

[2] *Instituto Nacional de Pesquisas da Amazonia (INPA), Manaus-AM, CEP 69083-000 Brazil.*

[3] *Institute of Physics, University of São Paulo, São Paulo 05508-900, Brazil.*

[4] *EWRE Division, Department of Civil Engineering, Indian Institute of Technology Madras, Chennai 600036, India.*

[5] *Institut für Angewandte Geowissenschaften, Technische Universität Darmstadt, Germany.*

[6] *Department of Biogeochemical Systems, Max Planck Institute for Biogeochemistry, 07701 Jena, Germany.*

[7] *John A. Paulson School of Engineering and Applied Sciences, Harvard University, Cambridge, MA, USA.*

[8] *Department of Earth and Planetary Sciences, Harvard University, Cambridge, MA, USA.*

[9] *St. Petersburg State University, 7/9 Universitetskaya nab, St. Petersburg, 199034, Russia.*

[10] *Instituto de Ciências Ambientais, Químicas e Farmacêuticas, Universidade Federal de São Paulo (UNIFESP), Diadema, SP, Brazil.*

[11] *Institut für Atmosphäre und Umwelt, Goethe Universität, 60438 Frankfurt, Germany.*

[12] *Biological, Environmental & Climate Sciences Department, Brookhaven National Laboratory, Upton, NY 11973-5000, USA.*

[13] *Scripps Institution of Oceanography, University of California San Diego, La Jolla, CA 92037, USA.*

[a] *now at Laboratoire de Météorologie Physique, Université Clermont Auvergne, Aubière, France.*

[b] *now at Institute of Agrarian Sciences, Federal University of Uberlândia, Uberlândia, Minas Gerais, Brazil.*

[c] *now at Institute for Climate and Global Change Research & School of Atmospheric Sciences, Nanjing University, Nanjing, 210093, China.*

[d] *now at Department of Chemistry, Snow College, Richfield, UT, USA.*

Correspondence to: M. Pöhlker (m.pohlker@mpic.de) and C. Pöhlker (c.pohlker@mpic.de)

Abstract

Size-resolved measurements of atmospheric aerosol and cloud condensation nuclei (CCN) concentrations and hygroscopicity were conducted at the remote Amazon Tall Tower Observatory (ATTO) in the central Amazon Basin over a full seasonal cycle (Mar 2014 - Feb 2015). In a companion part 1 paper, we presented an in-depth

5 CCN characterization based on annually as well as seasonally averaged time intervals and discuss different parametrization strategies to represent the Amazonian CCN cycling in modelling studies (M. Pöhlker et. al. 2016b). The present part 2 study analyzes the aerosol and CCN variability in original time resolution and, thus, resolves aerosol advection and transformation for the following case studies, which represent the most characteristic states of the Amazonian atmosphere:

10 *(1)* Near-pristine (NP) conditions, defined as the absence of detectable black carbon (< 0.01 µg m^{-3}), showed their highest occurrence (up to 30 %) in the wet season (i.e., Mar - May). On average, the NP episodes are characterized by a bimodal aerosol size distribution (strong Aitken mode: $D_{Ait} = 70$ nm, $N_{Ait} = {\sim}200$ cm^{-3} vs. weaker accumulation mode: $D_{acc} = 170$ nm, $N_{acc} = {\sim}60$ cm^{-3}), a mostly organic particle composition, and relatively low hygroscopicity levels ($\kappa_{Ait} = 0.12$ vs. $\kappa_{acc} = 0.18$). The NP CCN efficiency spectrum shows that

15 the CCN population is sensitive to changes in supersaturation (S) over a wide *S* range.

(2) Long-range transport (LRT) conditions frequently mix Saharan dust, African combustion smoke, and sea spray aerosols into the Amazonian wet season atmosphere. The LRT episodes (i.e., Feb - Apr) are characterized by an accumulation mode dominated size distribution ($D_{Ait} = 80$ nm, $N_{Ait} = 120$ cm^{-3} vs. $D_{acc} = 180$ nm, $N_{acc} = 300$ cm^{-3}), a clearly increased abundance of dust and salt compounds, and relatively high hygroscopic-

20 ity levels ($\kappa_{Ait} = 0.18$, $\kappa_{acc} = 0.34$). The LRT CCN efficiency spectrum shows that the CCN population is highly sensitive to changes in *S* in the low *S* regime.

(3) Biomass burning (BB) conditions dominate the Amazonian dry season. A selected characteristic BB episode shows a very strong accumulation mode ($D_{Ait} = 70$ nm, $N_{Ait} = {\sim}140$ cm^{-3} vs. $D_{acc} = 170$ nm, $N_{acc} = {\sim}3400$ cm^{-3}), particles with very high organic fractions (>90 %), and correspondingly low hygroscopicity levels ($\kappa_{Ait} =$

25 0.14, $\kappa_{acc} = 0.17$). The BB CCN efficiency spectrum shows that the CCN population is highly sensitive to changes in *S* in the low *S* regime.

(4) Mixed pollution conditions show the superposition of African (i.e., volcanic) and Amazonian (i.e., biomass burning) aerosol emissions during the dry season. The African aerosols showed a broad monomodal distribution ($D = 130$ nm, $N = {\sim}1300$ cm^{-3}), with very high sulfate fractions (20 %), and correspondingly high hy-

30 groscopicity ($\kappa_{Ait} = 0.14$, $\kappa_{acc} = 0.22$). This was superimposed by fresh smoke from nearby fires with one strong mode ($D = 113$ nm, $N_{acc} = {\sim}2800$ cm^{-3}), an organic-dominated aerosol, and sharply decreased hygroscopicity ($\kappa_{Ait} = 0.10$, $\kappa_{acc} = 0.20$). These conditions underline the rapidly changing pollution regimes with clear impacts on the aerosol and CCN properties.

Overall, this study provides detailed insights into the CCN cycling in relation to aerosol-cloud interaction in the

35 vulnerable and climate-relevant Amazon region. The detailed analysis of aerosol and CCN key properties and particularly the extracted CCN efficiency spectra with the associated fit parameters provide a basis for an in-depth analysis of aerosol-cloud interaction in the Amazon and beyond.

1 Introduction

Clouds are a key factor in the Earth's atmosphere and climate system (Bony et al., 2015). Thus, sound scientific knowledge on the life cycle and highly dynamic properties of clouds is of significant importance for our understanding of atmospheric cycling and climate change (Seinfeld et al., 2016). A number of recent overview studies summarize the various facets of aerosol-cloud-precipitation-climate interactions in a detailed and comprehensive way (e.g., Andreae and Rosenfeld, 2008; Tao et al., 2012; Rosenfeld et al., 2014).

The Amazon Basin and its unique rain forest ecosystem are fundamentally shaped by the intense and large-scale (re)circulation of water between biosphere and atmosphere. Accordingly, the life cycle of shallow and deep convective clouds in the Amazon has been subject of numerous previous studies (e.g., Andreae et al., 2004; Freud et al., 2008; Rosenfeld et al., 2016b; Wendisch et al., 2016; Braga et al., 2017). In particular, the extent of anthropogenic influence on cloud lifecycle through continuous land use change and combustion-related aerosol emissions has been actively debated (Roberts et al., 2003; Davidson et al., 2012; Goncalves et al., 2015). It is well established that the properties and dynamics of clouds can be fundamentally altered by changing cloud condensation nuclei (CCN) regimes, which are a fraction of the total (tropospheric) aerosol population (Rosenfeld et al., 2008; Reutter et al., 2009).

In terms of microphysical processes in cloud formation and development, the number concentration of CCN, $N_{CCN}(S)$, and the peak water vapor supersaturation, S, at the cloud base play a key role. Here, S is predominantly determined by the updraft velocity, w_b, of the adiabatically rising air parcel at the cloud base. Depending on $N_{CCN}(S)$ and S, a certain number of cloud droplets at the cloud base, N_{db}, is formed (Rosenfeld et al., 2016b). In the Amazon Basin, N_{db} ranges around few hundred particles per cubic centimeter for clean and between 1000 and 2000 cm^{-3} for polluted conditions (Rosenfeld et al., 2016a; Braga et al., 2017). Upon cloud development and rising air masses, the initial droplets grow by condensation of water vapor, which can be observed as changes in the cloud drop size distribution (DSD). Thus, the DSD is a function of thermodynamic parameters (i.e., the updraft velocity w), aerosol conditions (i.e., $N_{CCN}(S)$), and the cloud evolution (i.e., the cloud depth H). Important bulk DSD properties are, in particular the droplet number concentration, N_d, and the effective droplet radius r_e. For $r_e > 11$ µm, the probability of droplet collision and coalescence processes increases to significant levels and warm rain formation is initiated (Cecchini et al., 2017b).

A detailed analysis of the properties and variability of the Amazonian CCN population is a prerequisite for the understanding of cloud cycling in this region. However, the CCN data from the Basin is still sparse. Therefore, we conducted a systematic characterization of the trends and properties of the central Amazonian CCN population at the Amazon tall tower observatory (ATTO) site. The first half of this study has been published recently as part 1 (M. Pöhlker et al., 2016). The present manuscript represents part 2 of this endeavor and focuses on the variability and properties of periods that are characteristic for the Amazonian atmosphere.

1.1 Brief summary of companion part 1 paper

The part 1 paper (M. Pöhlker et al., 2016) focuses on the multi-month trends in the Amazonian CCN population by presenting data from a full seasonal cycle. In particular, it presents annually averages of the key CCN parameters, a detailed analysis of the specific seasonal as well as diurnal trends and a systematic analysis of different CCN parametrization schemes to represent the Amazonian CCN cycling in modeling studies.

The major findings of part 1 can be summarized as follows: (i) The CCN population in the central Amazon is predominantly defined by the overall aerosol concentration as well as the shape of the characteristic bimodal

aerosol size distribution in the CCN-relevant size range. Accordingly, a key property that has to be taken into account for the interpretation of the CCN results is the relative proportion of the Aitken and accumulation modes (mode maxima at $D_{Ait} \sim 70$ nm and $D_{Acc} \sim 150$ nm). (ii) The hygroscopicity parameters, $\kappa(S,D_a)$, of the two modes were found to be remarkably stable for most of the observation period ($\kappa_{Ait} = 0.14 \pm 0.03$ vs.

5      $\kappa_{Acc} = 0.22 \pm 0.05$) with only weak seasonal and no diel variability. Accordingly, we concluded in part 1 that the shape of the aerosol size distribution is the predominant factor, whereas $\kappa(S,D_a)$ is only of secondary importance for the variability in the Amazonian CCN population, in agreement with previous studies. (iii) Furthermore, part 1 summarizes the CCN key parameters that allow an efficient modeling of the Amazonian CCN population. The prediction of CCN concentrations is particularly reliable when time series of total aerosol concentration and/or

10   the aerosol size distribution are available. The data and parametrization schemes in part 1 will improve the representation of the Amazonian CCN cycling in future modeling studies.

As a particularly helpful concept, we emphasized CCN efficiency spectra, which can be regarded as 'CCN signatures' for a particular aerosol population, by describing their behavior for the atmospherically most relevant S range. Here, a rather simple analytical expression (i.e., a single- or double-error function fits) suffice to repre-

15   sent the essence of the CCN-relevant properties of an aerosol population, which includes the characteristic shape of the aerosol size distribution and the $\kappa(S,D_a)$ size dependence. Furthermore, the CCN efficiency spectra are independent of the total aerosol number concentration (in contrast to CCN spectra) and, thus, can flexibly be scaled to the concentration range of interest to obtain CCN concentrations at a certain S level. Finally and beyond their potential use in models as CCN parametrization, the shape of the CCN efficiency spectra is very instructive to

20   visualize the specific behavior of contrasting aerosol population in cloud formation. This aspect will be one focal point of the present study.

1.2   Aims and scope of this study

To complete the analysis started in part 1, this manuscript analyzes the CCN variability in original time resolu-

25   tion (~4.5 h), which is sufficient to resolve its short-term variability in relation to air mass changes as well as aerosol emission and transformation processes. In the present work, we will zoom into the long-term CCN data set in two steps: First, we discuss the aerosol and CCN variability for two contrasting 2-months periods that characterize the *pollution minimum* and *maximum* in relation to complementary, trace gas, and aerosol parameters. Second, we will analyze four case studies with a length of a few days that represent the following particularly inter-

30   esting and characteristic events/conditions in the central Amazon region: (i) the cleanest observed episodes, which can be regarded as a near-pristine atmospheric state, (ii) long-range transport (LRT) aerosol advection during the wet season, which typically brings Saharan dust, African combustion aerosols, as well as marine aerosol particles, (iii) advection of biomass burning smoke from large deforestation fires in southeast Basin after few days of atmospheric processing, and (iv) prevalence of mixed pollution from African LRT and local fires, repre-

35   senting a frequent pollution scenario at the ATTO site. In summary, the overall purpose of this study is to link the measured CCN abundance and properties with the characteristic emissions and transformation processes that govern the Amazonian aerosol population. With the CCN parametrization strategies, developed in part 1, we provide a basis for efficient CCN prediction under characteristic aerosol and CCN conditions in the Amazon Basin.

2 Experimental section

2.1 Aerosol and trace gas measurements at the ATTO site

The present study is mostly based on *in situ* measurements at the remote ATTO site, which has been described in detail by Andreae et al. (2015). Further relevant information regarding the site, the measurement period, and the

5   aerosol and trace gas instrumentation can be found in the part 1 paper by M. Pöhlker et al. (2016). Note that the time frame of the present analysis including the four in-depth case studies overlapped with the two intensive observation periods (IOPs) of international Green Ocean Amazon 2014/5 (GoAmazon2014/5) campaign (Martin et al., 2016a; 2016b). Specific details on the measurements of equivalent black carbon (BC_e) mass concentrations, M_{BCe}, with the multi-angle absorption photometer (MAAP) can be found in Saturno et al. (2016; 2017b). Specific

10   details on the measurements of the mole fraction of carbon monoxide (CO), c_{CO}, with a G1302 analyzer (Picarro Inc. Santa Clara, CA, USA) can be found in Winderlich et al. (2010).

      Details on the aerosol chemical speciation monitor (ACSM, Aerodyne Research Inc., Billerica, MA, USA) measurements, which provide online information on the mass concentrations, $M_{species}$, of organics (OA), sulfate (SO_4^{2-}), nitrate (NO_3^-), ammonium (NH_4^+), and chloride (Cl^-), can be found in Ng et al. (2011). A detailed de-

15   scription of the long-term operation of the ACSM at the ATTO site can be found in Carbone et al. (2017). For selected case study and seasonal time frames, we calculated the mean values of $M_{species}$ as well as corresponding mass fractions, $f_{species}$, according to

$$f_{species} = \frac{M_{species}}{M_{OA} + M_{SO4} + M_{NH4} + M_{NO3} + M_{Cl}}$$

Furthermore, predicted hygroscopicity parameters, κ_p, were calculated based on the ACSM results according to

20   Gunthe et al. (2009) by

$$\kappa_p = f_{OA} \cdot 0.1 \ + \ (1 - f_{OA}) \cdot 0.6$$

However, it has to be noted that M_{NH4} ranged below its detection limit (0.248 µg m^{-3}) during the clean Amazon wet season months, making the obtained results unreliable (the questionable periods are marked in Table 3, which is discussed later in this study). For these periods with questionable results, M_{NH4} was omitted in the cal-

25   culation of the mass fractions

$$f_{species} = \frac{M_{species}}{M_{OA} + M_{SO4} + M_{NO3} + M_{Cl}}$$

which has to be kept in mind in the interpretation of the results. Similarly, also κ_p was calculated with M_{NH4} being omitted. The nominal size range of the ACSM spans from 75 to 650 nm and the measurements are conducted size-integrated. Accordingly, the ACSM results tend to be dominated by larger particles with relatively high

30   masses, which makes the $M_{species}$ results more representative for the accumulation mode composition. Accordingly, the calculated κ_p was compared to the hygroscopicity parameter for the lowest measured S level, $\kappa(0.11\ \%)$, corresponding with the largest measured critical diameter D_a (~170 nm).

2.2 CCN measurements and data analysis

35   A detailed description of the operation of the CCN counter (CCNC) and the subsequent data analysis can be found in the companion paper (M. Pöhlker et al., 2016), which is the basis for the present study. For further CCN-relevant information, we refer the reader to Rose et al. (2008) and Krüger et al. (2014). The CCN efficiency spectra parameterization as introduced in part 1 plays a key role in the present manuscript. The single-error function (erf) fit (mode = 1) is represented by the following function

$$\frac{N_{CCN}(S)}{N_{CN,10}} = v_1 + a_1 \cdot erf\left(\frac{ln\frac{S}{S_1}}{w_1}\right)$$

with v_1 as offset, a_1 as prefactor, S_1 as the supersaturation, at which half of the maximum activated fraction (*MAF*) of the aerosol particles acts as CCN (e.g., 50 % for $v_1 = 0.5$), and w_1 as the width of the erf fit. To simplify the fitting procedure, $a_1 = 0.5$ was assumed. Further, $v_1 = 0.5$ can be used as an input parameter in most

5 cases. The combination, $a_1 = 0.5$ and $v_1 = 0.5$, yields convergence of the erf against unity, corresponding with an activation of all particles as CCN at high S, which is adequate in most cases. Analogously, the double-erf fit (mode = 2) is represented by the function

$$\frac{N_{CCN}(S)}{N_{CN,10}} = v_1 + a_1 \cdot erf\left(\frac{ln\frac{S}{S_1}}{w_1}\right) + a_2 \cdot erf\left(\frac{ln\frac{S}{S_2}}{w_2}\right)$$

with the index 1 and 2 specifying the variables for both modes. To simplify the fitting procedure, $a_1 = 0.5$ and

10 $v_1 = 0.5$ was assumed.

Another important aspect is worth mentioning: In part 1 we tested different reference aerosol number concentrations, $N_{CN,Dcut}$ (e.g., $N_{CN,10}$ and $N_{CN,50}$), for the CCN efficiency spectra parametrization. In this study, we use only one reference concentration for clarity – namely $N_{CN,10}$. The choice of $N_{CN,10}$ can be explained by the fact that it is experimentally rather easily accessible (e.g., via condensation particle counter, CPC, measure-

15 ments), whereas reference concentrations such as $N_{CN,50}$ require more elaborated experimental setups (e.g., scanning mobility particle sizer, SMPS, data).

2.3 Definition of near-pristine periods

Biomass and fossil fuel combustion have been the primary sources of pollution aerosols in the Amazon region.

20 Since combustion processes are always associated with the emission of black carbon (BC), the MAAP-derived BC_e serves as a primary marker for the presence of pollution aerosols in this study. Accordingly, we identified the cleanest aerosol conditions observed, which are called *near-pristine* periods throughout this study, as the absence of detectable BC_e. Petzold and Schönlinner (2004) determined the detection limit of the MAAP "as the minimum resolvable absorbance" by considering "the variability of blank filter optical properties". The detection

25 limit corresponds with the resulting mean absorbance of the blank filter + 3 times the standard deviation (std) resulting in an absorption coefficient of 0.132 Mm^{-1} for 30-min averages. The M_{BCe} was calculated by using mass absorption cross sections (MAC) retrieved by fitting MAAP absorption coefficients at 637 nm and single particle soot photometer (SP2) rBC mass measurements during the different seasons as explained in Saturno et al. (2017). Using the MAC values measured at the ATTO site (MAC for the wet season: 11.4 ± 1.2 m^2 g^{-1}; MAC for

30 the dry season: 12.3 ± 1.3 m^2 g^{-1}), the conversion to M_{BCe} corresponds to 0.011 – 0.012 µg m^{-3}. Note that this threshold would be higher if a "traditional" MAC value of 6.6 m^2 g^{-1} were used to calculate M_{BCe} (~0.019 µg m^{-3}). Here, we selected a threshold concentration of $M_{BCe}{}^* = 0.01$ µg m^{-3}, when the ATTO-specific MAC values are taken into account. Accordingly, near-pristine periods fulfill the criterion $M_{BCe} < M_{BCe}{}^*$ for ≥6 h (after applying a 5-point running average to the 1 h M_{BCe} data).

2.4 Backward trajectories

The systematic back trajectory (BT) analysis and classification in this study has been adopted from C. Pöhlker et al. (2017), where an in-depth description of the procedure can be found. Briefly: The BT analysis is based on the hybrid single particle Lagrangian integrated trajectory model (HYSPLIT, NOAA-ARL) with meteorological in-

5   put data from the global data assimilation system (GDAS1) (Draxler and Hess, 1998). Three-day BTs have been calculated every 1 h with a start height of 1000 m at the ATTO site for the time period of 1 Jan 2008 until 30 June 2016. A sensitivity test confirmed that start heights of the HYSPLIT back trajectories at 200 and 1000 m gave very similar results. Accordingly, the chosen start height at 1000 m appears to be a good representation of the origin of the boundary layer air masses. Subsequently, the resulting ensemble of 74,496 individual BTs has

10   been classified into 15 clusters with k-means cluster analysis (CA). The supplement Fig. S1 shows a map of the north-eastern Amazon Basin with the ATTO site and the mean track of the 15 BT clusters. It illustrates that the air masses arrive almost exclusively in a rather narrow easterly wind sector (between 45° and 120°). Within this sector, four BT subgroups can be identified: (i) a northeasterly (NE) track including the clusters NE1, NE2, and NE3, shown in bluish colors; (ii) an east-northeasterly (ENE) track including the clusters ENE1, ENE2, ENE3,

15   and ENE4, shown in greenish colors; (iii) an easterly (E) track including the clusters E1, E2, E3, and E4, shown in reddish colors; and (iv) a group of 'inland' trajectories in east-southeasterly (ESE) directions including clusters ESE1, ESE2, and ESE3 as well as one cluster towards the south-west (i.e., SW1). For a detailed characterization of the region, which is covered by the BTs and represents the ATTO site footprint with the trace gas, aerosol, and CCN sources that are presumably most relevant for the long-term observation at the ATTO site, we refer

20   the reader to C. Pöhlker et al. (2017).

2.5 Satellite data and analysis

The satellite data products used in this study were obtained from the NASA Giovanni web interface (http://giovanni.gsfc.nasa.gov/, last access 26 May 2017), developed and maintained by the NASA Goddard Earth Sciences

25   Data and Information Services Center (GES DISC) (Acker and Leptoukh, 2007). The following satellite products have been used:

- Cloud top temperature data (AIRX3STD_v006 product) from the atmospheric infrared sounder (AIRS) instruments on board of the satellites Terra (data included from 24 Feb 2002 to 30 Jun 2016) and Aqua (data included from 04 Jul 2002 to 30 Jun 2016) satellites. For the corresponding time series in this study, the

30   Aqua and Terra data were averaged per day for a representative region.

- Cloud cover data is obtained by the moderate resolution imaging spectroradiometers (MODIS) on board of the Terra (included data from 24 Feb 2002 to 30 Jun 2016) and Aqua (included data from 04 Jul 2002 to 30 Jun 2016) satellites. The obtained Aqua and Terra time series were averaged. Note that cloud cover strongly depends on the spatial resolution of the instrument as outlined in King et al. (2013).

35   - Cloud droplet effective radius, r_e, is calculated from the products measured from the MODIS instrument on board of Terra (included data from 24 Feb 2002 to 30 Jun 2016) and Aqua (included data from 04 Jul 2002 to 30 Jun 2016) satellites. Since r_e varies with vertical cloud development and total CCN abundance, we filtered the r_e data by cloud top temperature (King et al., 2013).

- Precipitation rate data, P_{TRMM}, from the tropical rainfall measuring mission (TRMM). The

40   TRMM_3B42_Daily_v7 product has been used for the time period 01 Jan 1998 until 30 Jun 2016.

The satellite data were used as time series of area averaged data products within a region of interest around the ATTO site (ROI$_{ATTO}$: 59.5° W to 54° W and 3.5° S to 2.4° N) as specified in Fig. S1.

2.6 Seasonal cycles of remote sensing and in situ data

5 To provide an overall picture of the seasonal cycle of selected aerosol and meteorological parameters representative for the ATTO region, various data sets were combined in Fig. 1. Remote sensing data products were used in the time frames outlined above. For M_{BCe}, c_{CO}, and $N_{CN,10}$, 4-6 years of ATTO site measurements were available. Additionally, M_{BCe} data measured at the ZF2 site, located 40 km NW of Manaus, were used to reflect the conditions back to 2008 (e.g., Martin et al., 2010a). In terms of sources and conditions, the ATTO and ZF2 sites are

10 comparable (C. Pöhlker et al., 2017). The c_{CO} data include ATTO site measurements from 2012 to 2017.

2.7 Aerosol sampling and scanning electron microscopy with x-ray spectroscopy

Aerosol samples for electron micro-spectroscopy were collected by impaction. A home-made single stage impactor (flow rate = 1-1.5 lpm; and nominal cut-off D_{cut} = ~500 nm) was used for collection. The collection effi-

15 ciency below D_{cut} decreases steeply, however, a certain fraction of particles in this size range is still collected. Moreover, a fraction of very small particles is additionally collected via diffusive deposition and therefore available for the microscopic analysis. Aerosol particles were deposited onto silicon nitride substrates (Si$_3$N$_4$, membrane width 500 µm, membrane thicknesses 100 or 150 nm, Silson Ltd., Northhampton, UK). Afterwards samples were stored in airtight containers at -20 °C immediately after sampling.

20 Without further treatment like sputter-coating, particles were analyzed in a high-resolution scanning electron microscope (SEM; FEI Quanta 200F, FEI, Eindhoven, The Netherlands). An acceleration voltage of 12.5 kV with a spot size of approximately 3 nm was used. X-ray emission was analyzed with an energy-dispersive X-ray analysis (EDX; Edax Genesis, Edax Inc.). The system is able to record characteristic X-ray emissions for all elements with Z > 5. Obviously, in the present work Si could not be quantified due to the silicon substrate (Kandler

25 et al., 2011).

3 Results and discussion

3.1 Aerosol and cloud microphysical seasonality in the Amazon

Prior to the in-depth analysis of the aerosol and CCN cycling for characteristic case studies, this section provides

30 an overview of the aerosol and cloud microphysical seasonality, representing the precipitation cycle in the ATTO region. The pollution markers c_{CO} and M_{BCe} in Fig. 1a show a pronounced seasonal cycle with a prevalence of clean conditions in the wet season vs. the biomass burning-related pollution maximum in the dry season (Andreae et al., 2015). The annual minimum in M_{BCe} levels occurred at the end of April (with a weekly M_{BCe} means of ~0.03 µg m^{-3}), whereas its highest concentrations were observed in August and September (with a

35 weekly M_{BCe} means of ~0.40 µg m^{-3}). The seasonal cycle of c_{CO} shows a temporal shift of about 1 month with its minimum in the beginning of June (with a weekly c_{CO} means ~100 ppb) and largest values from October to December (with a weekly c_{CO} means ~200 ppb). The phase shift between the c_{CO} and M_{BCe} seasonality can be explained by the complex spatiotemporal interplay of combustion-related BC and CO sources, aerosol wet scavenging, as well as alternating advection of Northern vs. Southern hemispheric (NH vs. SH) air masses (Martin et

40 al., 2010b; Andreae et al., 2012; 2015). Similar to the M_{BCe} trends, the total aerosol particle concentration $N_{CN,10}$ tracks the seasonality in biomass burning activities (in South America and Africa) with lowest concentrations in

March and April ($N_{\text{CN,10}}$ weekly means ~200-300 cm^{-3}) and highest values between August and November ($N_{\text{CN,10}}$ weekly means from 1000 to 2000 cm^{-3}) as shown in Fig 1b. The CCN concentration at a supersaturation of 0.5 %, $N_{\text{CCN}}(0.5\ \%)$, which was calculated based on long-term SMPS data and the κ-Köhler parametrization as outlined in our part 1 paper, mostly tracked the seasonal trends in $N_{\text{CN,10}}$. Its minimum around Mar and April

5   showed weekly mean $N_{\text{CCN}}(0.5\ \%)$ values around 200 cm^{-3}, whereas the maximum showed values between 1000 and 2000 cm^{-3}.

Figure 1c shows the seasonal cycles of two different precipitation related data products: First, the P_{TRMM} data, representing the area-averaged precipitation rate in the ROI$_{\text{ATTO}}$ (see Fig. S1). The P_{TRMM} data reveals a rather broad wet season precipitation maximum from March to May (defining the wet season from a meteorologi-

10   cal perspective). The smallest precipitation rates are observed from September to November. Second, the P_{BT} data represents the cumulative precipitation along the BTs arriving at the ATTO site (for details see C. Pöhlker et al., 2017). Thus, P_{BT} represents a measure for the extent of rain-related aerosol scavenging – particularly of long-range transport aerosols – upon air mass transport to the ATTO site. A pronounced maximum in P_{BT} and the related scavenging is observed for the months April and May, which coincides with the minimum in aerosol pa-

15   rameters (i.e., M_{BCe} and N_{CN}) (see also Moran-Zuloaga et al., 2017).

Figure 1d shows the seasonal cycles in cloud fraction and cloud top temperature for the ROI$_{\text{ATTO}}$. Both are predominantly influenced by the position of the intertropical convergence zone (ITCZ) with its belt of extended deep convective cloud systems and strong precipitation. According to Fig. 1d, the densest cloud cover and deepest convection (represented by lowest cloud top temperature) occurs upon northwards passage of the ITCZ in the

20   middle of the wet season (i.e., March and April) as well as upon southwards passage of the ITCZ at the end of the dry season (around November). The maximum in deep convection in March and April – expectedly – corresponds with the peak in P_{TRMM}. A global picture of the spatiotemporal trends in cloud microphysical properties can be found in King et al. (2013).

Figure 1e presents the satellite-derived effective radius r_{e} of liquid cloud droplets that links the seasonality in

25   aerosol and cloud properties. The r_{e} data have been filtered by cloud top temperature to discriminate the different r_{e} growth states in different heights of the convective clouds. It is well established that increased CCN loads entail an influence on cloud properties, which typically results in corresponding decrease in droplet diameter (e.g., Freud et al., 2008; Stevens and Feingold, 2009). Figure 1e underlines this trend by means of a pronounced seasonality in r_{e} with its maximum during clean wet season conditions (i.e., April and May) and its minimum during

30   the polluted months in the dry season (i.e., August to November). The detailed understanding of the impact of the CCN loading on the cloud microphysical properties, however, is the subject of ongoing studies.

The trends in Fig. 1 provide a coherent picture of the aerosol, cloud, and precipitation seasonality as well as their corresponding linkages. The following sections will zoom into this overall picture by presenting detailed aerosol and CCN data from characteristic wet and dry season conditions of the year 2014. The corresponding

35   months that are discussed in greater detail (April and May in Fig. 2 and August and September in Fig. 4) are highlight in Fig. 1 by a background shading to embed the corresponding observations into this overall picture.

3.2 Aerosol and CCN time series for representative wet season conditions

During Amazonian wet season (February to May), the influence of local and regional anthropogenic pollution

40   (i.e., from biomass and fossil fuel burning) decreases to a minimum and simultaneous strong precipitation causes efficient aerosol scavenging (see Fig. 1). The combination of both effects constitutes a comparatively clean state

of the Amazonian atmosphere (Martin et al., 2010b; Andreae et al., 2015). During this time of the year, biogenic aerosols from the surrounding rain forest ecosystem, such as secondary organic aerosol (SOA) from the oxidation of biogenic volatile organic compounds (BVOC) as well as primary biological aerosol particles (PBAP), prevail (Pöschl et al., 2010; Huffman et al., 2012; Yanez-Serrano et al., 2015). However, the regionally and biogenically dominated background state of the atmosphere is frequently perturbed by the episodic advection of long-range transport (LRT) aerosols from Africa in air masses that bypass the major rain fields and, therefore, 'survive' the intense scavenging (Moran-Zuloaga et al., 2017). The frequent intrusion of LRT aerosols is a characteristic feature during the Amazonian wet season and represents a strong and important impact on the Amazonian ecosystem (e.g., Chen et al., 2009; Bristow et al., 2010; Baars et al., 2011; Abouchami et al., 2013; Yu et al., 2015; Rizzolo et al., 2016). These LRT plumes mostly comprise a complex mixture of Saharan dust, African biomass burning smoke, and marine aerosols from the transatlantic air passage (e.g., Talbot et al., 1990; Swap et al., 1992; Glaser et al., 2015).

The 2-months period in Fig. 2 can be regarded as representative for typical wet season conditions in the ATTO region as it includes both scenarios: periods with the prevalence of the local (biogenic) background aerosol and episodes under the influence of LRT plumes, as well as intermediate states. In general, the wet season 2014 showed 'average hydrological conditions' without significant precipitation anomalies within the ROI_{ATTO}, which is in stark contrast to 2015/16 with its pronounced El Niño influence and an associated negative precipitation anomaly (see C. Pöhlker et al., 2017; Saturno et al., 2017b). Furthermore, the pollution tracers, N_{CN}, M_{BCe}, and c_{CO}, showed comparatively low values with concentrations around $N_{CN} = 330 \pm 130$ cm^{-3}, $M_{BCe} = 0.03 \pm 0.05$ µg m^{-3}, and $c_{CO} = 110 \pm 10$ ppb (given as mean $\pm$ 1 std for entire time period in Fig. 2) in agreement with previous studies (Andreae et al., 2012; Artaxo et al., 2013; Andreae et al., 2015). In terms of atmospheric circulation, the first half of the 2-month time frame was dominated by back trajectory arrivals from the north-east (blue and green BT clusters, see Fig. 2a and Fig. S1), whereas during the second half the dominant wind direction shifted towards easterly directions (orange and red BT clusters, see Fig. 2a and Fig. S1) (compare Andreae et al., 2015; Moran-Zuloaga et al., 2017). This gradual swing of the dominant wind direction from NH to SH relates to the northwards movement of the ITCZ.

Three episodes with detectable LRT influence occurred during the selected time period in Fig. 2 and have been called *LRT1*, *LRT2*, and *LRT3* in the context of this study (see Table 1). These episodes have been defined according to Moran-Zuloaga et al. (2017).[1] The question to what extent the Amazonian wet season approximates a pristine and pre-industrial state, which is unaffected by human activities, has been actively debated over the last years (Andreae, 2007; Martin et al., 2010b; Hamilton et al., 2014). Although the wet season is free from major pollution influence, there is evidently a persistent background pollution in varying states of dilution. Andreae et al. (2012) argued in this context that the "atmospheric state and processes in the Amazon Basin cannot be understood without the consideration of pollutant inputs by long-range transport". This is particularly true for gaseous compounds (e.g., CO), however, also a certain fraction of advected pollution aerosols may endure the intense wet deposition and reach the ATTO site. This statement is supported by Fig. 2, which shows comparably clean con-

---

[1] Moran-Zuloaga et al. (2017) showed that seven moderate to major LRT events occurred in the wet season 2014. Three of these seven LRT episodes overlap with the present CCN data and are called *LRT1*, *LRT2*, and *LRT3* in the context of this study. According to the nomenclature in Moran-Zuloaga et al. (2017), these events correspond to 2014_5, 2014_6, and 2014_7.

ditions (mean M_{BCe} ± 1 std: 0.013 ± 0.013 µg m^{-3}) for the extended period from 14 April until end of May. However, a closer inspection of the data shows several M_{BCe} peaks (some even exceeding 0.1 µg m^{-3}) that indicate the influence of diluted pollution plumes. Although (highly) diluted, these plumes impact the CCN population, as discussed in Sect. 3.4.

5   In order to shed light on this important aspect, we quantified the relative abundance of very clean periods in the ATTO region, which are called *near-pristine* (NP) in this study (see details in Sect. 2.3). A statistical overview of the relative fraction of near-pristine episodes for the years 2012 to 2017 is shown in Fig. 3. It shows that near-pristine conditions typically occur from March to May with their highest abundance around late April and early May when weekly frequencies of occurrence reach up to 30 % or more. Note that the near-pristine episodes
10   in 2014 mostly occurred in April and May, which is in good agreement with the multi-year trends. The individual near-pristine episodes in 2014 are represented as grey vertical shading in Fig. 2. Their frequency of occurrence clearly increased towards the end of the wet season, inversely related to the frequency of occurrence of the LRT events, which mostly occurred towards the beginning of the wet season (Moran-Zuloaga et al., 2017). For a detailed analysis in Sect. 3.4, we selected three of the longer (i.e., multi-day) near-pristine periods, which are
15   highlighted as *NP1*, *NP2*, and *NP3* in Fig. 2.

The following general picture emerges for the CCN parameters: The time series of the $\kappa(S,D_a)$ size distributions in Fig. 2d clearly illustrates the different $\kappa(S,D_a)$ of Aitken and accumulation modes as discussed in our part 1 study (M. Pöhlker et al., 2016). Overall, $\kappa(S,D_a)$ shows a clear variability for low S, representing the accumulation mode, and rather stable values for higher S, representing the Aitken mode (see Fig. 2h). The occurrence of
20   the LRT plumes stands out clearly by causing a significant enhancement of $\kappa(S,D_a)$ with κ_{Acc} reaching 0.4 and κ_{Ait} reaching 0.25 (see Fig. 2d and h). Moreover, the LRT events are also associated with increased $N_{CCN}(S)$ and $N_{CCN}(S)/N_{CN}$ values (Fig. 2g and i). Note that the occurrence of the LRT events precisely coincides with the minima in P_{BT}, and, thus, 'windows' in aerosol scavenging (compare Moran-Zuloaga et al., 2017).

For the extended and comparatively clean period from 14 April until end of May, the SMPS contour plot
25   (Fig. 2c) reveals equally strong Aiken and accumulation modes as well as a 'patchy' appearance, due to frequent rainfall causing (local) aerosol scavenging. As outlined in our part 1 study, the aerosol abundance in the particle size range >40 nm predominantly defined the measured CCN population (M. Pöhlker et al., 2016). Accordingly, the $N_{CCN}(S)$ and $N_{CCN}(S)/N_{CN}$ time series directly track the SMPS-derived patchy pattern. The low S levels – i.e., $N_{CCN}(0.11 \%)$ – which do not activate Aitken mode particles, closely followed the accumulation mode concentra-
30   tion, N_{acc}, time series, whereas the higher S levels (i.e., $N_{CCN}(1.10 \%)$), which also activated particles in the Aitken mode, closely tracked $N_{CN,10}$ (= $N_{Ait} + N_{acc}$). Two of the subsequent case studies will focus in more detail of the specific CCN properties of the *NP* (Sect. 3.4) and *LRT* (Sect. 3.5) cases (see also Table 1).

3.3 Aerosol and CCN time series for representative dry season conditions

35   During the dry season (August to November), the central Amazon is under continuous influence of pronounced anthropogenic pollution. The predominant type is biomass burning smoke from deforestation fires, which coined the term "biomass burning season" (Freud et al., 2008). In addition, various urban and industrial emission sources in eastern and southern Brazil as well as southern Africa may also contribute by hard-to-define quantities (e.g., Andreae et al., 1994; Saturno et al., 2017b). The minimum in precipitation rates and, thus, in aerosol scav-
40   enging fosters the distribution of pollution aerosols over large areas by extending their atmospheric lifetime (see Fig. 1).

Figure 4 represents the dry season pendant of Fig. 2 and shows the corresponding time series for a characteristic dry season period from 01 August until 30 September 2014. The BT clusters in Fig. 4a show that easterly and southeasterly BTs prevailed, since the ITCZ was located north of the ATTO site. The BT clusters, which are most characteristic for the dry season, approached the Amazon River delta from the southern Atlantic and then

5   follow the river in western direction towards the ATTO site (red and orange clusters, see Fig. S1). These 'dry season river BTs' are subject of more detailed discussion in the case study in Sect. 3.7. For certain episodes, the wind swings further to southeasterly directions and brings air masses from inland directions (black, brown, and grey BT clusters, see Fig. S1). These 'dry season inland BTs' are further discussed in the case study in Sect. 3.6.

In contrast to the wet season, the accumulation mode clearly dominates the size distribution, which explains

10 the increased CCN efficiencies, particularly at low S (Fig. 4c and i). The frequent 'pulses' in the accumulation mode concentration can be attributed to (aged) biomass burning plumes, which impact the ATTO site episodically (typically for few days) (see Freitas et al., 2005). The M_{BCe}, N_{CN}, and c_{CO} levels were typical for dry season conditions in the NE Amazon Basin with $M_{BCe} = 0.55 \pm 0.35\ \mu g\ m^{-3}$, $N_{CN} = 1520 \pm 780\ cm^{-3}$ and $c_{CO} = 140 \pm 50\ ppb$ (given as mean $\pm$ 1 std for the time period in Fig. 4) (e.g., Rissler et al., 2004; Andreae et al., 2012;

15 Artaxo et al., 2013; Andreae et al., 2015; Saturno et al., 2017b).

The most obvious event in Fig. 4 is the advection of a strong biomass burning (BB) plume from 17 to 23 August 2014 (the highest pollution levels that were observed during the entire CCN measurement period). This event can be recognized by means of strong pulses in N_{Acc}, M_{BCe}, and c_{CO} as well as a dip in $\kappa(S,D_a)$. The ACSM-derived organic-to-sulfate ratio confirms that the biomass burning pulse comprised a predominantly organic aer-

20 osol. In general, the measured $\kappa(S,D_a)$ levels respond inversely to the organic-to-sulfate ratio, confirming previous studies, which stated that organic matter and sulfate constituents are mostly defining the aerosol's hygroscopicity in the Amazon (Roberts et al., 2002; Gunthe et al., 2009). The major biomass burning plume in Aug 2014 is subject of the detailed case study *BB* in Sect. 3.6.

Beside this major biomass burning plume, several shorter pulses, which were supposedly also caused be up-

25 wind fires, were observed throughout the dry season period and their frequency of occurrence increased towards the end (i.e., after 12 Sep). Phenomenologically, the major and minor biomass burning plumes were similar as they exhibit peaks in N_{CN}, M_{BCe}, and c_{CO} and simultaneous dips in $\kappa(S,D_a)$ and the organic-to-sulfate ratio. The second half of September comprised interesting conditions with comparatively high sulfate concentrations and a sequence of short biomass burning plumes. Thus, this period is influenced by a mixture of different (pollution)

30 aerosol populations from African long-range transport and regional South American sources. A detailed description of the case study *MixPol* can be found on the in the Sect. 3.7.

Similar to the wet season, different $\kappa(S,D_a)$ levels for the Aitken and accumulation modes as well as comparably low $\kappa(S,D_a)$ variability over time ($\kappa_{Ait} = 0.14 \pm 0.03$ vs. $\kappa_{Acc} = 0.23 \pm 0.04$, covering the entire time period in Fig. 4d and h) were observed. The $MAF(S)$ values tend to reach unity, except for $MAF(0.11\ \%)$ under the influ-

35 ence of biomass burning smoke (i.e., for the smaller and major smoke plumes).

3.4   Case study *NP* on near-pristine conditions

Aerosol-cloud interactions remain to be the largest uncertainty in global climate models and a better understanding of a preindustrial atmospheric state would help considerably to reduce this uncertainty (Carslaw et al., 2013;

40 Seinfeld et al., 2016). Since the Amazonian wet season provides the rare chance to analyze episodes of very

clean *continental* conditions[2], this case study extracts the characteristic aerosol and CCN properties and trends during the near-pristine periods as defined in Sect. 2.3 (compare also Table 1). Along these lines, Fig. 5 zooms into three selected episodes – called *NP1*, *NP2*, and *NP3* as highlighted in Fig. 2 – and combines meteorological, aerosol, and CCN time series for a detailed analysis.

5   The meteorological parameters in Fig. 5a, b, and c illustrate typical wet season conditions: (i) a rather high degree of cloudiness, which can be seen by means of the strong cloud-related dimming of the incoming short-wave radiation, SW_{in}, (ii) frequent local (P_{ATTO}) and regional (P_{TRMM}) rain events, (iii) a comparatively stable northeasterly wind direction, which is consistent with the BT analysis in Fig. 2, (iv) a rather constant wind speed, U, for most of the time, which was getting more vigorous during rain events, (v) high relative humidity (RH)

10   conditions, being inversely related to SW_{in} and reaching saturation during the nights, and (vi) a characteristic time series of the equivalent potential temperature, θ_e, which tracked the daily onset of solar heating (see simultaneous increase of SW_{in} and θ_e) and further provides valuable information on vertical atmospheric mixing, particularly in connection with rain events. Specifically, sudden drops in θ_e indicate a downward transport of air masses from upper tropospheric layers, which occurred frequently with the onset of strong rain (for more details

15   see Wang et al., 2016).

The corresponding aerosol cycling is shown as aerosol number size distribution (dN/dlog$D$) contour plot in Fig. 5d. Under near-pristine conditions (i.e., grey shading) we found a dominant Aitken mode and a comparatively weak accumulation mode as reported previously (e.g., Andreae et al., 2015; M. Pöhlker et al., 2016). Moreover, the Aitken and accumulation modes reveal a patchy and discontinuous abundance with rather sudden

20   concentration increases and drops. These observations can be explained by a combination of different effects and processes: *First*, the strong and persistent (mostly combustion-related) sources of accumulation mode aerosol particles, which are responsible for the continuous and dominant accumulation mode in the dry season, were absent.

Second, the frequent rain events acted as an efficient aerosol removal mechanism via aerosol rain-out (i.e.,

25   particle activation into cloud/rain droplets) and wash-out (i.e., particle collection by falling droplets below clouds). The wash-out efficiency is slightly higher (~ factor 1.5) for Aitken than accumulation mode particles (Wang et al., 2010; Zikova and Zdimal, 2016). In contrast, the rain-out efficiency, corresponding to CCN activation, is typically much higher for accumulation than Aitken mode particles (M. Pöhlker et al., 2016). Accordingly, the rain pulses strongly modulated the aerosol's abundance via sudden and efficient deposition, which is

30   visible in Fig. 5d as characteristic 'notches' in the aerosol contour plot. The notches represent the (removed) part of the aerosol size fraction that was activated as CCN into cloud droplets. Illustrative examples can be found during days with strong rain showers, such as 27 April, 05 May, and 06 May. Note that the 'depth of the notches', corresponding to the smallest activated particles, could in principle be used to estimate the S levels during the corresponding events (compare procedure in Krüger et al., 2014). Further note in this context that besides deple-

35   tion of the accumulation relative to the Aitken mode, aerosol activation and *cloud processing* are known to also foster the opposite effect: The growth of Aitken mode particles into the accumulation mode via formation of aqueous phase reaction products (i.e., sulfate and aqueous phase SOA) in the cloud droplets, followed by droplet

---

[2] Note that this refers only to very clean continental conditions within the wet season hydrological regime. Very clean conditions within the dry season hydrological regime, which may differ substantially from the wet season scenario due to a contrasting (micro)meteorology, are not experimentally accessible due to the persistent character of the combustion-related aerosols and trace gases.

re-evaporation and deposition of the newly formed compounds onto the particles (e.g., Ervens, 2015; Farmer et al., 2015). Possibly, during 07 May, cloud processing was responsible for the formation of a rather strong accumulation mode from an existing Aitken mode population (Fig. 5).

As a *third* process, the Aitken mode population in the rain forest boundary layer (BL) was frequently replenished by pulse-like appearance of particles with diameters <50 nm. These events are supposed to be rain-related downward transport of air masses from an upper troposphere (UT) particle pool and the subsequent growth of the injected fine particles (Wang et al., 2016; Andreae et al., 2017). Remarkably, the combination of all these effects results in a comparatively constant total particle abundance N_{CN} across the rain showers, due to compensating effects of accumulation mode particle losses and simultaneous increases in Aitken mode abundance (see details in Wang et al., 2016). The rain-related downward transport of fine UT particles and their subsequent growth – presumably by the condensation of low-volatility vapors – is a characteristic feature of the Amazonian wet season. At least three pronounced examples for this process are included in the time frame of Fig. 5 (i.e., 27/28 April, 04/05 May, and 16/17 May). After their injection into the forests BL, the fine particles (initial diameters between 20 and 50 nm for the events in Fig. 5) reveal a "banana-like" growth into the Aitken mode size range (~70 nm) in the course of about 12-24 h. For the events in Fig. 5, we calculated an initial, and thus maximum, growth rate of 0.6 to 6 nm h^{-1}, which agrees well with the 1 to 6 nm h^{-1}, as reported by Kulmala et al. (2004) for tropical regions as well as the reported 5 nm h^{-1} in Zhou et al. (2002) for an Amazonian site. Note that these 'Amazonian bananas' differ from the classical new particle formation (NPF) that has been reported for various continental sites (i.e., in Northern temperate regions) (Kulmala et al., 2004), since number concentrations are lower by orders of magnitude and their nucleation and initial growth does not occur in the BL, but in the UT (Ekman et al., 2008; Engstrom et al., 2008; Pöschl et al., 2010; Andreae et al., 2017). Accordingly, the UT particle population that is frequently injected into the BL is already aged to a certain extent and, thus, presumably reflects chemical processes different from the atmospheric chemistry in the BL. The physicochemical details of the UT nucleation and growth are still largely unknown and subject of ongoing research (e.g., Andreae et al., 2017).

The CCN properties during near-pristine conditions are represented by time series of $\kappa(S,D_a)$ size distributions (Fig. 5d) and $N_{CCN}(S)$ for two selected S (Fig. 5e). The temporal pattern of the $\kappa(S,D_a)$ size distributions, which provides indications of the aerosol particles' chemical composition, reflects the 'pattern' of the underlying $dN/dlogD$ contour plot. Consistent with our observations in part 1 (M. Pöhlker et al., 2016), the accumulation mode reveals higher $\kappa(S,D_a)$ levels than the Aitken mode, likely due to chemical aging through cloud processing and a related increase in hygroscopicity (Farmer et al., 2015). The lowest $\kappa(S,D_a)$ levels were observed for the 'Amazonian bananas' (see Fig. 5d). Both, the accumulation and Aitken mode $\kappa(S,D_a)$ levels show a variability that tracks the Aitken and accumulation mode abundance. Note that $N_{CCN}(0.5\ \%)$ and particularly $N_{CCN}(0.2\ \%)$ show pronounced increases during periods with increased M_{BCe} levels (e.g., 25 April, 05 May, and 17 May). This underlines the remarkable impact of diluted pollution on the CCN population in an aerosol limited regime according to Reutter et al. (2009).

Figure 6a and b summarize the average aerosol and CCN key properties under near-pristine conditions. Figure 6a shows the characteristic average $N_{CN}(D)$ size distribution with a pronounced bimodal appearance, comprising a dominant Aitken mode ($D_{Ait} = 67 \pm 1$ nm, $N_{Ait} = \sim200$ cm^{-3}) and a comparatively weak accumulation mode ($D_{acc} = 171 \pm 2$ nm, $N_{acc} = \sim60$ cm^{-3}) (see Table 2). This bimodal shape mode is typical for clean Amazonian conditions as reported previously (e.g., Gunthe et al., 2009) and notably resembles aerosol size distributions during marine background conditions (e.g., Atwood et al., 2017). The corresponding $N_{CCN}(S,D)$ size distributions

for all S levels show that for S < 0.3 % mostly accumulation mode particles were activated, whereas for S > 0.3 % the Aitken mode particles also acted as CCN. Furthermore, Fig. 6a shows the average $\kappa(S,D_a)$ size dependence with a characteristic step-wise increase of $\kappa(S,D_a)$ towards larger D. The Aitken mode $\kappa(S,D_a)$ levels are rather low and sharply defined (mean ± std: 0.12 ± 0.01), whereas the accumulation mode $\kappa(S,D_a)$ levels are

5 slightly higher (0.18 ± 0.02). The results suggest that the Aitken mode particles, which are frequently injected into the BL via downward transport from the UT, mostly comprised organic matter. This observation agrees well with recent results showing that "the UT particles consist predominantly of organic material, with minor amounts of nitrate and very small fractions of sulfate" (Andreae et al., 2017). The hygroscopicity of organic material, κ_{org}, is typically assumed as ~0.10, however can vary substantially (close to 0 up to 0.3) as a function of the organic

10 material and its oxygen-to-carbon (O:C) ratio (Jimenez et al., 2009; Thalman et al., 2017). The $\kappa(S,D_a)$ levels of the accumulation mode similarly indicate the presence of predominantly organic particles, however with somewhat more inorganic constituents than in the Aitken mode. This is consistent with the corresponding ACSM results in Table 3, underlining that organic matter accounts for most of the mass (89 %), whereas nitrate (4 %) and sulfate (6 %) add only small contributions. Note that M_{NH4} ranged below detection limit for NP conditions and its

15 contributions was omitted in the calculation of the mass fractions accordingly (see Sect. 2.1). A predicted average hygroscopicity parameter, κ_p, of 0.16 ± 0.05 was calculated based on the ACSM results – excluding the questionable M_{NH4} – and agrees with the measured value of $\kappa(0.11 \%) = 0.19 \pm 0.05$ (Table 3).

Figure 6b displays the CCN efficiency spectrum for near-pristine conditions, which can be regarded as *CCN signature* of the corresponding aerosol population (for details refer to the companion part 1 paper). The pro-

20 nounced bimodal particle size distribution with its characteristic Hoppel minimum and the step-wise increase of $\kappa(S,D_a)$ (see Fig. 6a) result in a weak plateau at about $S = 0.4$ %, which required to apply a double-erf fit. For comparison, we also applied a single-erf fit. Expectedly, the double-erf fit is the better representation of the experimental data, although the single-erf fit also covers the data reasonably well, since the plateau is not particularly pronounced. However, a closer look reveals differences between the single- vs. double-erf fits for small and

25 large S. In the small S range (<0.1 %), the double-erf fit indicates that the NP aerosol particles start acting as CCN only above a minimum threshold at about $S = 0.06$ %. One possible physical explanation of this behavior could be the absence of suitable CCN in the size range of several hundred nanometers, which are indeed comparatively sparse under NP conditions according to Fig. 5. However, this size range was not covered directly by our CCN measurements, making it hard to draw solid conclusions. In the large S range (>1 %), the spectrum has not

30 reached full activation yet and keeps increasing. Since the double-erf fit describes the data more accurately than the single-erf fit, its extrapolation for S > 1.2 % is likely more accurate and suggests that 'full' activation (~90 %) is reached at S ~ 1.7 %. A CCN efficiency spectrum, representing very clean "green ocean" conditions at another Amazonian site from previous measurements[3], has been added to Fig. 6b for comparison and show very good agreement with our results (Roberts et al., 2001; Andreae et al., 2004).

35 The CCN efficiency spectra represent an instructive tool to visualize characteristic differences in the behavior of certain (contrasting) aerosol populations in cloud formation. Of particular relevance is the slope of the CCN efficiency spectra, $d(N_{CCN}(S)/N_{CN,10})/dS$ as the sensitivity of the activated CCN fraction of a given aerosol

---

[3] Data is taken from the CLAIRE 1998 campaign (28 March to 15 April 1998), conducted close to the village of Balbina, northeast of Manaus, Brazil.

population within a given S range to changes in supersaturation, ΔS. Accordingly, high $\mathrm{d}(N_{\mathrm{CCN}}(S)/N_{\mathrm{CN,10}})/\mathrm{d}S$ levels indicate a regime, in which already subtle a ΔS has relatively strong effects on the $N_{\mathrm{CCN}}(S)$ and, thus, N_{d} concentrations (assuming constant $N_{\mathrm{CN,10}}$), whereas low $\mathrm{d}(N_{\mathrm{CCN}}(S)/N_{\mathrm{CN,10}})/\mathrm{d}S$ levels indicate a regime that is characterized by rather stable $N_{\mathrm{CCN}}(S)$ and N_{d} concentrations, even upon large ΔS. This perception of CCN efficiency

5   spectra stands in certain analogy to a concept introduced by Reutter et al. (2009), which classifies the sensitivity of N_{d} concentrations in response to changes in N_{CN} and w_{b}. This results in three distinct regimes: (i) an *aerosol-limited* regime, which is characterized by high $S_{\max}$ (>0.5 %), a high $w_{\mathrm{b}}/N_{\mathrm{CN}}$ ratio, high activated fractions $N_{\mathrm{d}}/N_{\mathrm{CN}}$, and a linear relationship between N_{CN} and N_{d}; (ii) an *updraft-limited* regime, which is characterized by rather low $S_{\max}$ (<0.2 %), a low $w_{\mathrm{b}}/N_{\mathrm{CN}}$ ratio, low activated fractions $N_{\mathrm{d}}/N_{\mathrm{CN}}$, and a linear relationship between w_{b}

10   and N_{d}; and (iii) a *transitional* regime with intermediate states and non-linear dependencies of N_{d} on N_{CN} and w_{b}. Note that the concept by Reutter et al. has been developed for the conditions of pyro-convective clouds and, thus, represents an extreme case, which has to be kept in mind in the subsequent comparison with the CCN efficiency spectra.[4] Based on Reutter et al., NP conditions with the associated low aerosol concentrations ($N_{\mathrm{CN,10}} = 270 \pm 100$ cm^{-3}, Table 4) can be characterized as aerosol-limited, due to the overall low abundance of

15   potential CCN. However, the CCN efficiency spectrum in Fig. 6b suggests that the NP aerosol population *also* has a certain sensitivity to w_{b}, since changes in updraft velocity Δw_{b} – and the associated ΔS (even for S > 1 %) – largely modulate the activated fraction $N_{\mathrm{CCN}}(S)/N_{\mathrm{CN,10}}$. In this sense, the NP CCN efficiency spectrum has a very characteristic shape and differs clearly from the other case studies, as it keeps increasing over a wide S range with a somewhat larger slope for S < 0.3 % and a slightly decreasing slope for S > 0.3 %. Accordingly, the NP

20   case appears to be aerosol- *and* updraft-sensitive, which makes the corresponding aerosol-cloud interaction highly dynamic. For more quantitative insights, modelling runs according to Reutter et al. based on the characteristic NP bimodal $N_{\mathrm{CN}}(D)$ size distribution in Fig. 6a (in contrast to the monomodal accumulation mode, taken into account for the pyro-convective conditions) as well as adjusted N_{CN} and w_{b} ranges are required.

25   ## 3.5 Case study *LRT* on Saharan dust influence

The African continent is of significant importance for the Amazonian atmospheric composition as it represents a major source of desert dust and pollution aerosols (e.g., Swap et al., 1992; Andreae et al., 1994; Yu et al., 2015; Rizzolo et al., 2016). A systematic overview of the properties and relevance of LRT plume arrival in the ATTO region during the Amazonian wet season can be found in Moran-Zuloaga et al. (2017). Furthermore, a general

30   characterization of the CCN population's response to LRT conditions can be found in our part 1 paper (M. Pöhlker et al., 2016). Based on these previous studies, the present paper analyzes the characteristic impact of LRT plumes on the CCN population in detail.

The characteristic impact of LRT plumes on the aerosol and CCN data can already be seen in Fig. 2 by means of the episodes *LRT1*, *LRT2*, and *LRT3*. For a detailed analysis, the *LRT3* episode – as a particularly in-

35   structive example – has been chosen and is represented in Fig. 7 by selected meteorological, aerosol, and CCN

---

[4] The cloud parcel modelling by Reutter et al. (2009) was conducted for the specific case of pyro-convective conditions, developing over strong fires. Accordingly, a typical (monomodal) biomass burning aerosol size distribution with an accumulation mode maximum at 120 nm was used. In this sense, the study is bound to rather specific and extreme conditions. However, Reutter et al. state that the "key features of the three regimes of CCN activation (…) are not specific for young biomass burning aerosols and pyro-convective conditions but likely to apply also for other types of aerosols and meteorological conditions".

time series.[5] The layout of Fig. 7 is identical to the corresponding figures of the other case studies for clarity and comparability. Note that the advected dust plumes typically cause substantial increases in both, the coarse mode, which plays a secondary role here, and the accumulation mode, which explains their relevance for the CCN cycling (Moran-Zuloaga et al., 2017). The LRT influence is clearly visible in Fig. 7 by means of increases in M_{BCe}

5 (due to the LRT plume's smoke component), the accumulation mode abundance in the dN/dlog$D$ contour plot, the concentrations N_{CN} and $N_{CCN}(S)$ as well as in $\kappa(S,D_a)$.

The plume's influence on the ATTO site lasted for about four days with its onset on 09 April ~12:00 and its end on 13 April ~12:00, which is in good agreement with the corresponding remote sensing data in Moran-Zuloaga et al. (2017). During these four days, meteorology determined the variability of the LRT aerosol in the rain

10 forest BL via air mass advection (i.e., wind speed and direction), rain-related scavenging (i.e., P_{ATTO} and P_{TRMM}), and convective mixing (i.e., represented by SW$_{in}$ as a proxy). Throughout the *LRT3* period, the dominant wind direction was mostly NE to E, which is characteristic for wet season conditions (compare Fig. 2). Note that the BTs arriving from the NE are particularly prone to bring dust-laden air into the ATTO region (Moran-Zuloaga et al., 2017). Furthermore, only few (major) rain events and related aerosol scavenging occurred during this time,

15 which is a further prerequisite for efficient LRT transport. The arrival of the *LRT3* plume during afternoon hours of 09 April occurred via convective downward mixing of the aerosol into the forest BL (see simultaneous increases in SW$_{in}$, θ_e, and the accumulation mode in dN/dlog$D$) and its influence lasted until 13 April, when the concentration time series decreased gradually. Note that the advected LRT plumes are transported into the ATTO region as compact and stratified aerosol layers up to altitudes of 2-3 km (Moran-Zuloaga et al., 2017). Aerosol

20 concentrations were highest during the afternoon hours on 09, 10 and 11 April, when convection (see SW$_{in}$) is most efficient in mixing the aerosols downward into the BL. Furthermore, a sudden rain-related air mass change lasting for about 12 h (see wind direction and θ_e changes) in the end of 09 April/beginning of 10 April was associated with a simultaneous drop in LRT aerosol concentrations. The CCN population responded noticeably to the injection of the LRT pulses, which can be seen in $N_{CCN}(S)$, $N_{CCN}(S)/N_{CN,10}$, and $\kappa(S,D_a)$ in Fig. 2. Figure 7 dis-

25 plays the $N_{CCN}(0.2\ \%)$ and $N_{CCN}(0.5\ \%)$ time series, which show a two- to threefold increase upon LRT aerosol intrusion. Moreover, the $\kappa(S,D_a)$ data can be used as an indirect measure for the aerosol chemical composition, which primarily reflects the average ratio of organic vs. inorganic constituents in the particles. In Fig. 7d, the occurrence of elevated $\kappa(S,D_a)$ levels coincides exactly with the variability in dN/dlog$D$. For this particular event, κ_{Acc} increased from ~0.3 to ~0.4, whereas κ_{Ait} increased from ~0.15 to ~0.25.

30 Figure 6c summarizes the characteristic $N_{CN}(D)$ and $N_{CCN}(S,D)$ size distributions as well as the size dependence of $\kappa(S,D_a)$ during LRT influence. In general, the comparison of Fig. 6a and c contrasts the characteristic LRT vs. NP conditions and emphasizes that the intrusion of African LRT plumes into the wet season BL has significant influence on the aerosol and CCN population. Specifically, the accumulation mode under LRT conditions ($D_{acc} = 178 \pm 2$ nm, $N_{acc} = $ ~300 cm^{-3}) is about 5 times enhanced in comparison to the NP episodes. The Ait-

35 ken mode ($D_{Ait} = 77 \pm 2$ nm, $N_{Ait} = $ ~120 cm^{-3}), which appears in the LRT $N_{CN}(D)$ distribution only as a shoulder, shows comparable absolute strength as under NP conditions (see Table 2). The $N_{CCN}(S,D)$ size distributions show that supersaturations S ≤ 0.3 % activate particles mostly in the accumulation mode range, whereas S > 0.3 % starts activating the Aitken mode population. The $\kappa(S,D_a)$ size distribution shows κ_{Acc} reaching rather high levels

---

[5] Note that the *LRT3* event has also been chosen for in-depth case study analysis in Moran-Zuloaga et al. (2017), where it is called 2014_7. Accordingly, a number of additional aspects and observations concerning the *LRT3* event, which are not explicitly discussed in this work, can be found there.

up to 0.40 (κ_{Acc} = 0.34 ± 0.04) and κ_{Ait} with values up to 0.2 (κ_{Ait} = 0.18 ± 0.02). In comparison to the NP conditions, κ_{Acc} was clearly enhanced due to the presence of aged, internally mixed and salt-rich particles (see discussion in subsequent section). In contrast, the κ_{Ait} levels were only slightly higher than during the NP periods, probably due to a broader accumulation mode base, which reached into the Aitken mode range. Note that the relative

5   increase in $\kappa(S,D_a)$ for the contrasting LRT and NP conditions is large enough to exert an influence on the CCN population, which is an exceptional case throughout the Amazonian seasons, since the $\kappa(S,D_a)$ levels for most of the year vary within a rather narrow range (0.1 to 0.2) (see part 1 paper).

The African LRT plumes that frequently impact the Amazon Basin during the wet season comprise a complex mixture of different aerosols components, including (i) a fraction of Saharan dust (mostly >1 µm), (ii) bio-

10 mass burning aerosols from fires in the Sahel region (mostly in the accumulation mode), and (iii) marine aerosols from the plume's transatlantic passage (in coarse and accumulation modes) (Andreae et al., 1986; Talbot et al., 1990; Swap et al., 1992). Fresh soot and uncoated dust particles typically have low hygroscopicities, whereas sea salt particles (i.e., NaCl and sulfates) represent comparatively efficient CCN. The LRT plumes encounter a rather long atmospheric journey – about 10 days according to Gläser et al. (2015) – which is associated with strong at-

15 mospheric processing and typically results in complex internally mixed particles (see Andreae et al., 1986). The resulting mixtures of dust and salt as well as coated soot particles, as commonly found in the dust plumes, readily act as CCN at realistic S levels (<1 %) (Andreae and Rosenfeld, 2008).

Table 3 summarizes the ACSM results on aerosol chemical composition during LRT influence.[6] Note that the ACSM only measures the non-refractory fraction of the particle mass and, thus, does not detect a large frac-

20 tions of the dust and salt constituents. During LRT conditions and with respect to the non-refractory part, organic mass dominated the particle composition (73 %), with minor nitrate contributions (3 %) and larger fractions of ammonium (12 %)[7] and sulfate (10 %). Furthermore, a sea salt-related increase in detected chloride mass (4 %) relative to the NP state was observed. Based on the ACSM results, a predicted κ_p, of 0.24 ± 0.16 was obtained, which agrees reasonably well with the measured hygroscopicity level $\kappa(0.11\ \%)$ = 0.35 ± 0.04. Accordingly, the

25 observed elevated fractions of sulfate and ammonium were responsible for part of the increase in $\kappa(S,D_a)$. The remaining difference between κ_p and $\kappa(0.11\ \%)$ can likely be explained by further refractory inorganics that were not covered by the ACSM. As an illustration of the complex mixing state of the African LRT aerosol population, Fig. S2 and S3 provide selected SEM-EDX data from a characteristic LRT aerosol sample. Note that these results merely serve as a *qualitative example* here, whereas a quantitative microspectroscopic analysis of LRT

30 samples is subject of ongoing work. The observed particles' morphology underlines the influence of atmospheric processing and shows a high degree of internal mixing. Chemically, the EDX maps show dust particles, sulfate salts, as well as a rather large abundance of NaCl particles.

Figure 6d displays the characteristic CCN efficiency spectrum for the LRT conditions, which – expectedly – shows a rather steep increase at low S due to two effects pointing in the same direction: an enhanced accumula-

35 tion mode and the presence of rather 'good' CCN with comparatively high $\kappa(S,D_a)$ levels. This large initial slope

---

[6] ACSM data was available from Aug 2014 to Sep 2016. Accordingly, the ACSM time frame does not cover the *LRT1*, *LRT2*, and *LRT3* events, which are discussed in detail in this work. Instead, we analyzed the ACSM data for 12 comparable LRT episodes in 2015 and 2016 according to Moran-Zuloaga et al. (2017) (see also Table 1).
[7] Ammonium mass concentrations are only slightly above detection limit and, thus, the results have to be considered carefully.

corresponds with a very small value for the characteristic variable $S_1 = 0.09$ %, which shows that at comparatively low S (lowest S_1 among all analyzed cases) already 50 % of the aerosol population were activated as CCN (Table 4). At S levels around 0.3 % already ~80 % of the aerosols acted as CCN, 'full' activation (90%) is already reached for $S = $ ~0.5 %. At higher S (i.e., > 0.9 %) the efficiency spectrum approaches unity. This is in
5   stark contrast to the near-pristine CCN efficiency spectrum in Fig. 6b, where 50 % of the particles were activated at significantly higher S around 0.5 %, whereas 'full' activation (90%) was hardly reached at high S around 1.7 %. Thus, the LRT episodes show a pronounced sensitivity to ΔS only in the low S regime, in contrast to the near pristine case with a sensitivity to ΔS spanning across a wide S range. With the characteristic shape of the CCN efficiency spectrum (i.e., rather strong accumulation mode) and the low aerosol concentrations
10   ($N_{CN,10} = 440 \pm 100$ cm^{-3}, Table 4) taken into account, the LRT episodes appear to be aerosol-limited according to Reutter et al. (2009).

3.6 Case study *BB* on biomass burning smoke

During the dry season, the ATTO site is frequently influenced by smoke from biomass burning (BB) activities in
15   different regions of the Amazon forest (Freitas et al., 2005; Andreae et al., 2012; 2015; C. Pöhlker et al., 2017). As a characteristic example, the case study *BB* focuses on the strong biomass burning plume that was observed at the ATTO site in the middle of August 2014. During this event, pollution aerosol and trace gas concentrations reached their annual maxima with $N_{CN,10}$ peaking at 5000 cm^{-3}, c_{CO} at 350 ppb, and M_{BCe} reaching up to 2.5 µg m^{-3}, as shown in Fig. 4. Selected meteorological, aerosol, and CCN time series of the event are shown in Fig. 8.
20   This case study provides the fortunate opportunity to analyze the CCN properties of *aged smoke* from a rather defined large-scale BB plume in the Amazon region.

Figure 8 shows that the influence of biomass burning smoke on the ATTO site lasted for about 6 days (17 to 23 August) with a rather gradual onset and decay. In terms of meteorology, this period was characterized by mostly cloud-free conditions (see SW_{in}) without precipitation, comparatively low RH levels, and some variability
25   in wind direction. Note that during the presence of this major smoke plume, an atmospheric dimming in the ATTO region could be recognized (i.e., compare SW_{in} maxima for the seven consecutive days). The signature of the smoke aerosol particles can very clearly be seen in the dN/dlog$D$ contour plot, N_{CN}, as well as M_{BCe}. In terms of particle size, the pronounced increase mostly occurred in the accumulation mode, which appears to be comparatively broad for this specific event. The CCN concentrations – e.g., $N_{CCN}(0.2$ %) and $N_{CCN}(0.5$ %) – track the
30   relative increase in total aerosol abundance and show a 4 to 5-fold increase as well. At the same time, the presence of the pyrogenic aerosols correspond to a clear drop in aerosol hygroscopicity in both, the Aitken ($\Delta\kappa_{Ait} \approx -0.05$) and accumulation modes ($\Delta\kappa_{Acc} \approx -0.1$) (see overlay of $\kappa(S,D_a)$ size distributions and the dN/dlog$D$ contour plot in Fig. 8d). This drop in $\kappa(S,D_a)$ is associated with a high organic-to-sulfate, OA/SO$_4^{2-}$, ratio (Fig. 8f), reflecting the dominant role of organic constituents in biomass burning particles as documented in previous studies
35   (Fuzzi et al., 2007; Artaxo et al., 2013; Lathem et al., 2013).

Geographically, the location of the fires and, thus, the origin of the strong biomass burning plume could be found by means of a combination of BTs and satellite data products as shown in Fig. S4 (Draxler and Hess, 1998; Acker and Leptoukh, 2007; Justice et al., 2011). The strong pollution at the ATTO site resulted from the presence of intense fires in the southern Amazon and a temporary 'swing' of the BT track over the fire locations.
40   During the dry season, the BTs mostly belong to the E and ESE clusters (see Fig. S1 and 4). For the period before and after the biomass burning plume, the BT track follows a 'coastal path' and enters the continent in the

region of the Amazon River delta (about 0° N 50° W). Subsequently, the air masses 'follow' the Amazon River in western directions to the ATTO site. During the peak period of the *BB* event the BTs deviate from the 'coastal path' and follow an 'inland path' across the southeast of Brazil (see Fig. S4a and Fig. 4). At about 7° S and 55°

5   W, the BTs intersect a region with strong fire activities, which are clearly visible in satellite products such as NO_2 total column measurements. These fires are localized along the Cuiabá-Santarém highway (BR-163). This highway corridor is known as a region of intense logging and burning of primary forest and its conversion to cattle pasture (Nepstad et al., 2002; Fearnside, 2007; C. Pöhlker et al., 2017). The transport time of the smoke from the fires to the ATTO site is about 2-3 days (given by the BTs), which provides a reference for the residence time and aging of the aerosol particles in the atmosphere. The satellite image in Fig. S4b shows the smoke plume that

10   originated in the BR-163 region and traveled northwestwards. It clearly impacts the area around Manaus and the ATTO site precisely during the 'event days' in August.

        For further characterization of the *BB* case study, we calculated a ratio of excess $N_{CN,10}$ to excess c_{CO} ($\Delta N_{CN,10}/\Delta c_{CO}$) for the event of 17.9 ± 0.7 cm^{-3} ppb^{-1} (see Fig. S5a), which agrees well with the typical range for a variety of vegetation fires (30 ± 15 cm^{-3} ppb^{-1}), in contrast to much higher $\Delta N_{CN,10}/\Delta c_{CO}$ levels for urban

15   ($100 – 300$ cm^{-3} ppb^{-1}) and power plant emissions (up to 900 cm^{-3} ppb^{-1}) (Janhaell et al., 2010; Kuhn et al., 2010; Andreae et al., 2012). Furthermore, the ratios of excess $N_{CCN}(S)$ to excess c_{CO}, $\Delta N_{CCN}(S)/\Delta c_{CO}$, for the individual S levels range between 6.7 ± 0.5 cm^{-3} ppb^{-1} for the lowest $S = 0.11$ % and values around 18.0 ± 1.3 cm^{-3} ppb^{-1} for higher S (see Table S1 and Fig. S5b). The $\Delta N_{CCN}(S)/\Delta c_{CO}$ ratios converge against $\Delta N_{CN}/\Delta c_{CO}$ already for comparably small S (i.e., > 0.24 %), which can be explained by the fact that small S already activate a substantial frac-

20   tion of the pronounced (mostly pyrogenic) accumulation mode (see discussion below). Kuhn et al. (2010) reported $\Delta N_{CCN}(0.6\%)/\Delta c_{CO}$ ratios around 26 cm^{-3} ppb^{-1} for biomass burning plumes and around 49 cm^{-3} ppb^{-1} for urban plumes, which is consistent with our observations. The obtained $\Delta N_{CCN}(S)/\Delta c_{CO}$ ratios were utilized in a dedicated CCN parameterization scheme in our part 1 study (M. Pöhlker et al., 2016).

        Figure 6e summarizes the corresponding N_{CN} and $N_{CCN}(S)$ size distributions as well as the size dependence

25   of $\kappa(S,D_a)$ for the *BB* case study. It shows a very strong accumulation mode $D_{acc} = 167 \pm 1$ nm, $N_{acc} = \sim3400$ cm^{-3}), 'swamping' the Aitken mode $D_{Ait} = 70 \pm 1$ nm, $N_{Ait} = \sim140$ cm^{-3}) almost completely, giving the entire distribution a monomodal appearance. It can be seen that already comparatively low S levels activate substantial fractions of the *BB* particle population. For $S < 0.5$ % almost the entire aerosol population is activated as CCN. The averaged $\kappa(S,D_a)$ levels are rather low for both, the Aitken and accumulation modes ($\kappa_{Ait} = 0.14 \pm 0.01$ and

30     $\kappa_{acc} = 0.17 \pm 0.02$), in which κ_{Acc} belongs to the lowest values found in the accumulation mode size range throughout the entire study. The low $\kappa(S,D_a)$ levels can be explained by the fact that pyrogenic aerosols predominantly contain organic constituents and rather low levels of inorganic species. The ACSM results during the *BB* period emphasize the predominant mass fraction of organics (91 %) as well as the minor contribution by nitrate (2 %), ammonium (3 %), and sulfate (4 %) (Table 3). The predicted κ_p of 0.14 ± 0.02 agrees reasonably well

35   with the measurement result $\kappa(0.10 \%) = 0.18 \pm 0.01$.

        Figure 6f displays the characteristic CCN efficiency spectrum for the *BB* period, which levels out clearly below unity. The grey line shows the erf fit treated to go from zero to one, which obviously does not match the data points for large S. The red line is an erf fit of the data where the plateau is an open fit parameter.[8] This erf fit

---

[8] The single erf fit with the pre-defined variable $v_1 = 0.5$ and $a_1 = 0.5$, which is an inappropriate representation of the experimental data, has been included here for consistency, since the assumption that the activated fraction reaches 100 % worked well for all other case studies.

matches the data points very well and the fit parameters as presented in Table 4 reveal the plateau at 93 %. Physically, this indicates the presence of an externally mixed aerosol population with 7 % of the particles being hydrophobic (e.g., fresh soot) and not acting as CCN in the measured S range. The slope of the efficiency spectrum shows a steep increase for $S < 0.4$ %, however, below $S \sim 0.05$ % no significant fraction of the particles can be

5   activated. Since this region is not covered by direct CCN measurements, this might be related to a large amount of accumulation mode particles with a low hygroscopicity. According to these findings, the ΔS sensitive range is rather small, spanning from ~ 0.05 % to ~ 0.4 %. According to Reutter et al. (2009), the *BB* case study conditions with the large number of available CCN (e.g., $N_{CCN}(0.47 \%) > 4000$ cm^{-3}) fall into the updraft-limited regime.

Generally, the large aerosol load, its optical properties, and its ability to serve as CCN might already influ-

10   ence cloud properties and stratification of the thermodynamic profile of the atmosphere at both, local and regional scales (Cecchini et al., 2017a). As mentioned above, the incoming solar radiation was dimmed compared to the days before and after this *BB* event. Furthermore, the cloud fraction decreased, which might result from stabilizing the atmosphere due to increased absorption of solar radiation in and above the boundary layer (Koren et al., 2004; Rosenfeld et al., 2008; Rosario et al., 2013). A detailed investigation of the direct radiative forcing

15   and the modification of cloud properties by aerosol particles in the Amazon rain forest are clearly beyond the scope of this study. Nevertheless, the results shown here may serve as input for dedicated regional climate simulations.

3.7   Case study *MixPol* on the complexity of the dry season aerosol population

20   This *MixPol* case study, which represents a scenario of *mixed pollution*, focusses on a 7-day period in September 2014 with an exceptionally low OA/SO$_4^{2-}$ mass ratio of about 3 (Table 3). Previous studies pointed out that the dry season atmosphere in the Amazon is typically dominated by smoke emissions from deforestation fires in the Basin (Freud et al., 2008; Artaxo et al., 2013). This is widely correct, however, upon deeper inspection the picture becomes more complex, since the contributions of further anthropogenic pollution types (i.e., fossil fuel

25   combustion, industry etc.) as well as natural sources (i.e., marine aerosol, biogenic emissions) to the dry season aerosol population have to be taken into account (C. Pöhlker et al., 2017; Saturno et al., 2017b). The significance of these additional non-biomass burning-related sources has not yet been quantified conclusively. Accordingly, the purpose of this case study is to shed exemplary light on the complexity of the dry season aerosol population by means of the present *MixPol* case study period. This analysis will underline and discuss the mixture of super-

30   imposed aerosol types, the comparatively high variability of aerosol key parameters, and the characteristic differences between long-range transport perturbed dry season conditions and superimposed regional emission pulses. Ultimately, these observations are discussed in the light of the related CCN cycling.

Meteorologically, the time frame of *MixPol* was mostly cloud-free (see daily profile in SW$_{in}$) and without precipitation (see P_{TRMM} and P_{ATTO}) as well as characterized by rather stable wind conditions (Fig. 9). With re-

35   spect to the aerosol and CCN parameters, the relevant time series, such as N_{CN}, M_{BCe}, $N_{CCN}(S)$, show a comparatively high variability. Specifically, the dN/dlog$D$ contour plot shows an alternating pattern: On one hand and marked by a grey shading, rather extended periods with comparably low aerosol concentrations (around 1000 cm^{-3}) and high $\kappa(S,D_a)$ values (up to 0.35) can be observed. The $\kappa(S,D_a)$ levels reaching ~ 0.35 are among the highest in the entire dry season 2014 (compare Fig. 4). On the other hand and marked by a purple shading,

40   these conditions are interrupted by several *pulses* with strongly enhanced aerosol concentrations (up to 5000 cm^{-3}) as well as substantially lower $\kappa(S,D_a)$ values (around 0.1). The changes in $\kappa(S,D_a)$ occur with simultaneous

changes in the aerosol chemical composition: Slight increases of the OA/SO$_4^{2-}$ ratio indicates that the pulses comprise organic-rich aerosol (purple shading, called *low κ* conditions), whereas the lower OA/SO$_4^{2-}$ aerosol is comparatively rich in sulfate (grey shading, called *high κ* conditions).

A combination of BTs and satellite data during the *MixPol* period shows that all BTs follow an easterly di-
5   rection along the Amazon River (Fig. S6), which is the most frequent scenario during the dry season as outlined in a recent study (C. Pöhlker et al., 2017). The same study also shows that during this period, the shores of the Amazon River can be regarded as the core region of the ATTO site footprint, where BT densities are highest. Accordingly, all aerosol and trace gas sources in these areas are of primary importance for the ATTO region. For instance, this is true for a deforestation hotspot in the area around the cities Oriximina and Obidos as well as a
10   variety of anthropogenic sources (i.e., industry, power plants, cities, shipping) (compare Fig. S6 and C. Pöhlker et al., 2017). During the *MixPol* time frame, several (smaller) deforestation fires were observed within the fetch of the corresponding BTs (Fig. S6). These fires, which mostly burnt for less than a day according to satellite ob-servation, are likely responsible for the 'low $\kappa(S,D_a)$ and increased OA/SO$_4^{2-}$ pulses' within the *MixPol* period. Thus, the pulses can be considered as the advection of near-by biomass burning plumes into the ATTO region.
15   According to the BT data, the smoke experienced a transport and aging time of 12-18 h. Thus, the smoke plumes during *MixPol* are fresher than during the *BB* case study, which experienced atmospheric aging for 2-3 days. In-terestingly, this difference in aging could

potentially be related to differences in the corresponding $\kappa(S,D_a)$ values with fresh smoke during *MixPol* show-ing a lower hygroscopicity ($\kappa_{Ait,MixPol}$ = ~0.10, $\kappa_{Acc,MixPol}$ = ~0.14) and the aged smoke showing higher values
20   ($\kappa_{Ait,BB}$ = ~0.14, $\kappa_{Acc,BB}$ = ~0.17).

Besides the rather short biomass burning smoke pulses, the sulfate-rich background aerosols must have orig-inated from other sources, since the relative sulfate contents in biomass burning smoke are typically below 6-7 %, which can be seen for instance by means of the *BB* case in Table 3 (see also Fuzzi et al., 2007; Gunthe et al., 2009). Several anthropogenic sources within the ATTO site footprint, such as industrial emissions, power
25   plants, and/or ship traffic on the Amazon River could potentially be responsible for the sulfate emissions. Fur-thermore, the sulfate-rich aerosol could be imported from African sources, such as oilrigs and related activities in the Gulf of Guinea. For the particularly high sulfate contents during *MixPol*, Saturno et al. (2017a) provided evi-dence that volcanic activities (i.e., Nyiragongo and Nyamuragira volcanoes in Eastern Congo) had an important influence here. Furthermore, Fioletov et al. (2016) indicated that these African volcanoes are major sulfur diox-
30   ide, SO$_2$, sources, even on a global scale, and, thus candidates for SO$_2$ and sulfate export towards the Amazon Basin. Generally, the background aerosol population during *MixPol* can be considered as a mixture of aged aero-sols from Africa and South America, which are mixed and processed in the transport air masses *en route*. While a quantification of the individual contributions is far beyond the scope of this paper, it illustrates the complexity of the dry season aerosol population with potential biomass burning, urban, industrial, and volcanic contribu-
35   tions.

Figure 6g and h summarize the $N_{CN}(D)$, $N_{CCN}(S,D)$, and $\kappa(S,D_a)$ size distributions during *MixPol*, separately for the biomass burning pulses (*low κ* with increased OA/SO$_4^{2-}$ ≈ 4) and LRT pollution (*high κ* with lower OA/SO$_4^{2-}$ ≈ 3). In both cases, the size distributions show a broad monomodal distribution, which did not allow a stable double log-normal mode fitting of Aitken and accumulation modes (see Table 2). This mode is centered at
40   ~135 nm for the (aged) LRT sulfate-rich aerosol, whereas the relatively fresh biomass burning smoke shows a modal diameter of ~113 nm, in agreement with ~100 nm for fresh biomass burning smoke reported by Andreae

et al. (2004). The corresponding $N_{CCN}(S,D)$ size distributions show similar shapes, however, substantial absolute differences in CCN concentration occurred. Furthermore, clear differences are also observed for the average $\kappa(S,D_a)$ size distributions: During the *high κ* conditions, $\kappa(S,D_a)$ shows a pronounced size dependence. The average hygroscopicity parameter <100 nm is rather size independent ($\kappa_{<100nm} = 0.14 \pm 0.01$). Instead, the average

5    $\kappa_{>100nm}$ increases with D up to 0.26 (on average: $\kappa_{>100nm} = 0.22 \pm 0.03$). According to the shape of the $\kappa(S,D_a)$ size distribution in Fig. 6g, it can be assumed that the aerosol hygroscopicity was even higher for D larger than the covered size range here (i.e., >170 nm). During the dry season, the highest $\kappa(S,D_a)$ levels for accumulation mode particles were observed during the peak abundance of sulfate at the ATTO site. The hygroscopicity during the *low κ* pulses shows generally lower values and weaker size dependence for particles smaller than 150 nm. The

10   average $\kappa_{<150nm} = 0.10 \pm 0.01$ was even smaller than during *BB* and *NP* cases and represents one of the lowest values measured during the entire observation period. For larger particles (e.g., >150 nm) $\kappa(S,D_a)$ strongly increased towards values comparable to those during the *high κ* events indicating that both 'events' are rather superimposed than alternating (on average: $\kappa_{>150nm} = 0.20 \pm 0.04$).

       Figure 6i shows the CCN efficiency spectra for the two *MixPol* states. The slope for the *high κ* state is sig-

15   nificantly steeper compared to the slope of the *low κ* pulses. The S_1 level of 50 % activation (0.16 %) for the sulfate-rich aerosol population is clearly lower than during the short biomass burning pulses (0.28 %). This rather large difference can be explained by the smaller modal diameter of the *low κ* relative to the *high κ* case. Furthermore, κ is significantly decreased for the biomass burning pulses, which are dominated by organic constituents. However, note that the absolute CCN concentration given by N_{CCN} is – while being less hygroscopic – signifi-

20   cantly higher for the organic-rich periods (for S > 0.07 %).

       In general, the *MixPol* case study emphasizes the following aspects: (i) The dry season aerosols that arrive at the ATTO site can be rather complex mixtures of superimposed emissions from different sources with contrasting chemical properties. (ii) The properties of the aerosol and CCN population can change rather suddenly and substantially (see N_{CN} and $N_{CCN}(S)$ changes by factor of 3-4 within few hours). Similarly, the aerosol hygro-

25   scopicity can vary rather strongly from the lowest value observed in the entire study (~0.1) to values around 0.35 and higher, which belong to the largest values observed here during the dry season. These quickly and substantially changing aerosol regimes will presumably also impact the cloud conditions during dry season. (iii) Finally, the Amazonian aerosol and CCN population can be substantially perturbed by emissions from sources (i.e., volcanoes in the Eastern Congo) that are remarkably far away from the ATTO site (~10,000 km) (Saturno et al.,

30   2017a). This emphasizes very clearly that intercontinental influences have to be considered carefully in the analysis of the Amazonian atmospheric composition.

3.8 Overview of CCN efficiency spectra

       CCN efficiency spectra represent an effective strategy to summarize the CCN properties of a certain aerosol pop-

35   ulation and, thus, can be regarded as *CCN signatures*. This last section provides a synoptic overview of the CCN efficiency spectra of all analyzed conditions by combining the case study-specific spectra from the present work with the seasonally averaged spectra from the companion part 1 study as well as spectra from a previous study (Andreae et al., 2004). The direct comparison allows to extract characteristic similarities, differences and trends, which could be linked to a concluding discussion on aerosol-cloud-interactions. Figure 10a combines all relevant

40   spectra for a wide S range. For clarity throughout the discussion, we subdivided the S range according to Reutter et al. (2009) into a low S ($S < 0.2$ %), a high S ($S > 0.5$ %), and an intermediate S (0.2 % $< S < 0.5$ %) regime.

Furthermore, we marked the range, in which average peak supersaturations at cloud base, $S_{cloud}(D_H, \kappa)$, in the ATTO region are expected. The $S_{cloud}(D_H, \kappa)$ results were obtained according to Krüger et al. (2014) and can be found in our part 1 study as well as in Table 2 of the present work. The relevant $S_{cloud}(D_H, \kappa)$ range spans from ~0.18 % to ~0.34 % and, thus, overlaps with the interphase between low and intermediate S regimes. Note that

5   the case study-specific CCN efficiency spectra in Fig. 10a allow an easy conversion into average CCN spectra by multiplication with the case study average N_{CN} results (Table 4). The resulting case study-specific CCN spectra are shown in Fig. S7.

Generally, the array of spectra in Fig. 10a spans a certain range of different shapes (see also Farmer et al., 2015). Within this range, the *NP* case study represents the lower limiting case with the 'slowest' increase in acti-

10   vated fractions (e.g., 50 % activation reached at S ~ 0.5 %). In contrast, the *BB* and *LRT* case studies represent the upper limiting cases, reaching high activated fractions 'quickly' (50 % activation at S ~ 0.15 % for *BB* case and at 0.09 % for *LRT* case, respectively). As a general observation, the trends among the case study spectra corresponds well with the trends among the seasonally averaged spectra (e.g., relationship between wet vs. dust seasons and NP vs. LRT case studies). However, certain features appear more emphasized in the case studies than in

15   the seasonal averages (e.g., steeper slope at S < 0.05 % for LRT season than LRT case study) due to the fact that the case studies incorporate more defined aerosol plumes and/or populations. As an example, the *LRT season spectrum* includes several LRT pulses, however, also clean periods in between (see part 1 study), whereas the *LRT case study* spectrum includes one 'pure' LRT pulse (see Table 1).

Within the low S regime, which corresponds with the activation of accumulation mode particles, the follow-

20   ing features stand out: The aerosol populations that act as CCN most efficiently – means at very low S < 0.05 % – are those with high κ levels, such as the sea salt-rich *LRT* and sulfate-rich *MixPol/high κ* populations. The aerosol population that acts as CCN least efficient is the NP case, which is characterized by a small fraction of accumulation mode particles with rather low κ. In between these extremes, the *BB* aerosol population is activated rapidly, once a threshold value of ~0.05 % is exceeded. Further note that all spectra have their largest slopes

25    $d(N_{CCN}(S)/N_{CN,10})/dS$ within the low S regime, which means that the activated fractions of all aerosol populations are most sensitive to ΔS in this range. In the intermediate S regime, corresponding to the activation of particles at the interphase of Aitken and accumulation modes (i.e., Hoppel minimum size range), the individual spectra show their highest divergence – means largest differences in CCN efficiency at a given S. In this range also the ATTO-relevant $S_{cloud}(D_H, \kappa)$ levels are located. Thus, the important $S_{cloud}(D_H, \kappa)$ range covers those S conditions that re-

30   veal the largest variability in activated fraction for the contrasting aerosol populations (e.g., *BB* vs. *NP* cases). In the high S range, all spectra show their smallest slopes and, thus, lowest sensitivity towards ΔS.

Figure 10a may serve as a basis for dedicated cloud-microphysical studies on the characteristic differences between the aerosol/CCN populations and their impacts on cloud properties. As a particularly relevant aspect, the results obtained here (i.e., N_{CN} concentrations and CCN efficiency spectra) can be used to investigate the sensi-

35   tivity of clouds under NP conditions, as an approximation of a pre-industrial state of the atmosphere. There are evidently large differences between NP background conditions and perturbed atmospheric states related to anthropogenic (aged) BB smoke in terms of total aerosol concentration as well as the shape of the CCN efficiency spectra. Similarly, the differences between the NP and LRT case studies suggest that the frequent LRT pulses in the wet season are related to simultaneous changes in the cloud microphysical state, although changes in total

40   aerosol concentration are small.

Since the size and composition of aerosol particles change dynamically due to atmospheric aging and processing, evidently, also the CCN spectra change accordingly. Figure 10b emphasizes the dynamic character of the CCN efficiency spectra's shape by means of different aging states of biomass burning plumes. Here we combined four biomass burning-related CCN efficiency spectra: (i) the *BB* case study spectrum, which represents

5   smoke after ~2-3 days of atmospheric aging (see Fig. S4), (ii) the *MixPol/low κ* case study spectrum, which represents smoke after ~1 day of aging (see Fig. S6), (iii) "cloud-processed smoke" from biomass burning regions in southeast Brazil after hours to days of atmospheric aging according to Andreae et al. (2004), and (iv) "fresh smoke in the mixed layer", also from southeastern Brazil, which was sampled in the fire plumes and, thus, was aged for minutes to hours (Andreae et al., 2004). Clearly, the shape of the spectra in Fig. 10b is very different.

10 The lowest activated fractions were observed for the fresh smoke (50 % activation at $S \sim 0.96$ %; 90 % at $S \sim$ 3.6 %), followed by the "cloud-processed smoke" (50 % activation at $S \sim 0.45$ %; converges against 86 %), then the *MixPol/low κ* case study spectrum (50 % activation at $S \sim 0.28$ %; 90 % at $S \sim 1.2$ %), and finally the *BB* case study spectrum (50 % activation at $S \sim 0.15$ %; 90 % at $S \sim 0.46$ %) with highest activated fractions as upper limiting case.

15 Atmospheric aging tends to increase the particle size through coagulation and condensational growth as well as enhances the particle's hygroscopicity through oxidation, aqueous phase chemistry, and reaction product deposition. In other words, aging tends to increase the strength of the accumulation at the expense of the Aitken mode and increases κ. Accordingly, it evolves the smoke's CCN efficiency spectra from the "fresh smoke" conditions – as the initial state – towards the *BB* case study conditions and presumably even further. This underlines

20 the well-known trend that atmospheric aging increases the suitability of a given particle population to act as CCN (Andreae and Rosenfeld, 2008). Important to note in the context of this study is the following: The CCN efficiency spectra represent signatures of a given aerosol population in a given state of atmospheric aging. Accordingly, the atmospheric aerosol aging and the dynamic evolution of the CCN efficiency spectra's shape has to be kept in mind upon discussion and utilization of the spectra in follow-up studies.

4 Summary and conclusions

In a recent synthesis paper on aerosol-cloud interaction and its highly uncertain representation in global climate models, Seinfeld et al. (2016) proposed that long-term and focused observations in "geographic areas that are critical in climate response" are necessary to obtain a detailed process understanding. Further, studies in "those

30 regions of the present-day atmosphere that approximate preindustrial conditions" will help to "replicate preindustrial aerosol-cloud relationships". In these regions – such as the Amazon Basin – clouds are particularly sensitive to small changes in CCN concentrations (Carslaw et al., 2013). Accordingly, observations are needed here to obtain crucial knowledge on the man-made perturbation of preindustrial aerosol cycling and cloud properties. This work aims to help tackling this major scientific challenge by presenting detailed long-term aerosol and CCN data

35 for characteristic atmospheric states at the Amazonian ATTO site, which is a unique, climate-relevant location with atmospheric conditions oscillation between near-pristine and anthropogenically strongly perturbed states.

The basis for this work are size-resolved measurements of atmospheric aerosol and cloud condensation nuclei (CCN) concentrations and hygroscopicity at the remote Amazon Tall Tower Observatory (ATTO) in the central Amazon Basin over a full seasonal cycle (Mar 2014 - Feb 2015). The results of these observations are

40 presented in two papers: The recently published part 1 paper provides an in-depth analyses of the multi-month trends in the Amazonian CCN population as well as seasonal averages of the CCN key parameters (M. Pöhlker et

al., 2016). Further, part 1 compares and discusses different CCN parametrization schemes and their suitability to represent the Amazonian CCN cycling in modelling studies. The present part 2 study completes this picture by analyzing the CCN variability in original time resolution (4.5 h), which is sufficient to resolve its short-term variability in relation to air mass changes as well as aerosol emission and transformation processes.

5 A focal point of both studies is the concept of CCN efficiency spectra, which represent an instruct-tive tool to visualize the different behaviors of contrasting aerosol populations in cloud formation and, thus can be regarded as 'CCN signatures'. Analytically, the CCN efficiency spectra can be described precisely and in a physically correct way by single- or double-error functions (erf). In contrast to other common analytical functions, the erf approach describes the measurement results very accurately and allows to extrapolate CCN properties to ex-

10 perimentally hardly accessible supersaturations in the low and high S regimes.

Here, we zoom into the long-term CCN data in two steps: First, we discuss the aerosol and CCN variability for two 2-months periods that represent contrasting states in the aerosol, cloud microphysical, and precipitation seasonality in the central Amazon. The selected periods provide insights into the characteristic atmospheric cycling during the very clean wet season and the highly polluted dry season. Second, we focus on the following

15 four selected case study periods, which represent particularly relevant atmospheric states:

Near-pristine (NP) and, thus, approximately preindustrial conditions are one of the scientifically most relevant atmospheric states at the ATTO site. Here, we defined NP conditions as the absence of detectable black carbon concentrations (<0.01 µg m^{-3}) and found their predominant occurrence from March to May (peak at end of April/beginning of May with up to 30 % weekly abundance). Under NP conditions, aerosol concentrations were

20 very low (270 ± 100 cm^{-3}) and the aerosol population had a characteristic bimodal shape with a dominant Aitken and comparatively weak accumulation mode ($D_{Ait} = 67$ nm; $N_{Ait} = \sim200$ cm^{-3} vs. $D_{acc} = 171$ nm; $N_{acc} = \sim60$ cm^{-3}). The aerosol particles comprise mostly organic matter with minor amounts of inorganic constituents (OA: 0.64 µg m^{-3}, NO$_3^-$: 0.03 µg m^{-3}, SO$_4^{2-}$: 0.04 µg m^{-3}, Cl$^-$: 0.01 µg m^{-3}). The observed low $\kappa(S,D_a)$ levels agree with the particles' composition and show a certain size dependence ($\kappa_{Ait} = 0.12 \pm 0.01$ vs. $\kappa_{acc} = 0.18 \pm 0.02$). The

25 CCN efficiency spectrum shows a characteristic shape since it converges against full activation rather slowly (50 % activation at ~0.5 %, 90 % activation at ~1.7 %). Thus, the CCN population is sensitive towards ΔS in both, the low and high S regime. Accordingly, the CCN population can be regarded as both, aerosol sensitive due to the low total aerosol concentrations and updraft sensitive according to the CCN efficiency spectrum with its sensitivity to ΔS across a wide S range.

30 During *long-range transport* (LRT) episodes within the wet season, major amounts of aged Saharan dust, African biomass burning smoke, and Atlantic marine aerosols are advected pulse-wise into the Basin (mostly Feb - Apr). Total aerosol concentrations (440 ± 100 cm^{-3}) are slightly enhanced relative to the NP state and the aerosol population has a bimodal shape with a minor Aitken and a stronger accumulation mode ($D_{Ait} = 77$ nm, $N_{Ait} = \sim120$ cm^{-3} vs. $D_{acc} = 178$ nm, $N_{acc} = \sim300$ cm^{-3}). Beside the non-refractory fraction of organics and inor-

35 ganics (OA: 1.81 µg m^{-3}, NO$_3^-$: 0.08 µg m^{-3}, NH$_4^+$: 0.30 µg m^{-3}, SO$_4^{2-}$: 0.25 µg m^{-3}, Cl$^-$: 0.04 µg m^{-3}), a larger refractory fraction of mineral dust and sea salts can be found in internally mixed particles. The observed $\kappa(S,D_a)$ levels are increased compared to the NP state in agreement with the chemical composition ($\kappa_{Ait} = 0.18 \pm 0.02$ vs. $\kappa_{acc} = 0.34 \pm 0.04$). The CCN efficiency spectrum shows a steep increase – and thus high sensitivity to ΔS – at low S and quickly converges against full activation towards high S (50 % activation at ~0.09 %, 90 % activation

40 at ~0.53 %). Thus, the CCN regime under LRT influence can be regarded as aerosol limited.

Biomass burning (BB) is the predominant anthropogenic influence during the Amazonian dry season, which alters the atmospheric composition substantially. During the BB event analyzed here, we found strongly enhanced aerosol concentrations (3200 ± 1040 cm^{-3}) and an accumulation mode dominated size distribution ($D_{Ait} = 70$ nm, $N_{Ait} = \sim 140$ cm^{-3} vs. $D_{acc} = 167$ nm, $N_{acc} = \sim 3440$ cm^{-3}). The aged smoke particles comprise

5   mostly organic matter (OA: 19.1 µg m^{-3}, NO$_3^-$: 0.50 µg m^{-3}, NH$_4^+$: 0.54 µg m^{-3}, SO$_4^{2-}$: 0.79 µg m^{-3}, Cl$^-$: 0.03 µg m^{-3}). The observed $\kappa(S,D_a)$ levels were comparatively low and weakly size dependent ($\kappa_{Ait} = 0.14 \pm 0.01$ vs. $\kappa_{acc} = 0.17 \pm 0.02$). The corresponding CCN efficiency spectrum shows a rather steep increase at low S and converges against a threshold (~ 93 %) below full activation at high S (50 % activation at $S \sim 0.15$ %). With respect to the large particle concentrations and the large sensitivity of the CCN efficiency spectrum to ΔS in the

10   low S regime, the *BB* case falls into the updraft limited regime.

During the dry season, the central Amazon often experiences superimposed aerosol populations from regional, continental, and even trans-continental sources. Here, we analyzed a characteristic example of such *mixed pollution* (MixPol) scenarios, in which a mixture of African volcanic emissions and nearby Amazonian fires impacted the ATTO site: Under conditions with a predominant influence of the African volcanic emissions, we

15   found a broad monomodal size distribution ($D_{mode} = 135$ nm, $N_{mode} = \sim 1300$ cm^{-3}), strongly enhanced sulfate levels (OA: 5.48 µg m^{-3}, SO$_4^{2-}$: 1.76 µg m^{-3}), and correspondingly high hygroscopicities ($\kappa_{<100nm} = 0.14 \pm 0.01$ vs. $\kappa_{>100nm} = 0.22 \pm 0.03$). Under conditions with predominant influence by the nearby fires, we found high concentrations in a monomodal distribution ($D_{mode} = 113$ nm, $N_{mode} = \sim 2800$ cm^{-3}), an enhancement of organic matter on top of the sulfate background (OA: 8.08 µg m^{-3}, SO$_4^{2-}$: 2.05 µg m^{-3}), and low hygroscopicities

20   ($\kappa_{<150nm} = 0.10 \pm 0.01$ vs. $\kappa_{>150nm} = 0.20 \pm 0.04$). Accordingly, the interplay of the aged volcanic plume and the fresh smoke resulted in large variations of the total aerosol concentration, aerosol composition, and CCN properties. We suppose that the highly variable CCN population yields associated (microphysical) variations in cloud properties.

Finally, the CCN efficiency spectra for all analyzed cases are discussed in an overview, which emphasizes

25   the following differences, similarities and trends: (i) The array of all spectra span a range of variability, which represents the scope and diversity of CCN conditions in the central Amazon as a function of relevant S levels. (ii) Within this range, the estimated peak supersaturations at cloud base, $S_{cloud}(D_H,\kappa)$, are collocated with the intermediate S range (i.e., $0.2 - 0.5$ %), in which the CCN efficiency spectra shows their highest variability and, thus underlines the impact of changing aerosol populations on cloud properties. (iii) The sensitivity of the CCN popu-

30   lations to changes in S was highest within a low S regime ($S < 0.2$ %), whereas the lowest susceptibilities occurred in the high S regime ($S > 0.5$ %). (iv) The combination of CCN efficiency spectra for different, particularly contrasting, aerosol populations provides a basis for follow-up studies on the aerosol-related differences in cloud properties in the Amazon region and beyond. (v) Finally, the atmospheric aging of aerosol particles in the atmosphere is reflected into a corresponding evolution of the CCN efficiency spectra's shape and has to be kept

35   in mind upon their utilization.

5 Data availability

The data of the key results presented here (i.e., aerosol size distributions, κ levels, CCN efficiency spectra) has been deposited in supplementary tables for use in follow-up studies. For specific data requests or detailed information on the deposited data, please refer to the corresponding authors.

Acknowledgements

This work has been supported by the Max Planck Society (MPG) and the Max Planck Graduate Center with the Johannes Gutenberg University Mainz (MPGC). For the operation of the ATTO site, we acknowledge the support by the German Federal Ministry of Education and Research (BMBF contract 01LB1001A) and the Brazilian Ministério da Ciência, Tecnologia e Inovação (MCTI/FINEP contract 01.11.01248.00) as well as the Amazon State University (UEA), FAPEAM, LBA/INPA and SDS/CEUC/RDS-Uatumã. This work has been financial support from the German Research Foundation (DFG grant KA 2280/2); the St. Petersburg state University, Russia (project 11.37.220.2016) as well as the EU FP7 project BACCHUS (project no. 603445); the Sao Paulo Research Foundation (FAPESP grants 13/05014-0 and 13/50510-5); and the Atmospheic System Resarch program, US Department of Energy. This paper contains results of research conducted under the Technical/Scientific Cooperation Agreement between the National Institute for Amazonian Research, the State University of Amazonas, and the Max-Planck-Gesellschaft e.V.; the opinions expressed are the entire responsibility of the authors and not of the participating institutions. We highly acknowledge the support by the Instituto Nacional de Pesquisas da Amazônia (INPA). The Office of Biological and Environmental Research of the Office of Science is acknowledged for funding, specifically the Atmospheric Radiation Measurement (ARM) Climate Research Facility and the Atmospheric System Research (ASR) Program. We would like to especially thank all the people involved in the technical, logistical, and scientific support of the ATTO project, in particular Susan Trumbore, Carlos Alberto Quesada, Matthias Sörgel, Thomas Disper, Andrew Crozier, Bettina Weber, Nina Ruckteschler, Uwe Schulz, Steffen Schmidt, Antonio Ocimar Manzi, Alcides Camargo Ribeiro, Hermes Braga Xavier, Elton Mendes da Silva, Nagib Alberto de Castro Souza, Adir Vasconcelos Brandão, Amauri Rodriguês Perreira, Antonio Huxley Melo Nascimento, Thiago de Lima Xavier, Josué Ferreira de Souza, Roberta Pereira de Souza, Bruno Takeshi, and Wallace Rabelo Costa. We acknowledge the use of FIRMS data and imagery from the Land, Atmosphere Near real-time Capability for EOS (LANCE) system operated by the NASA/GSFC/Earth Science Data and Information System (ESDIS) with funding provided by NASA/HQ. Satellite product analyses and visualizations used in this paper were produced with the Giovanni online data system, developed and maintained by the NASA GES DISC. We also acknowledge the MODIS and OMI mission scientists and associated NASA personnel for the production of the data used in this research effort. Further, we thank the GoAmazon2014/5 team for the fruitful collaboration and discussions. Moreover, we thank Qiaoqiao Wang, Bruna Holanda, Oliver Lauer, Ovid O. Krüger, Maria Praß, Kathrin Reinmuth-Selzle, Daniel Rosenfeld, and J. Alex Huffman for support and stimulating discussions.

References

Abouchami, W., Nathe, K., Kumar, A., Galer, S. J. G., Jochum, K. P., Williams, E., Horbe, A. M. C., Rosa, J. W. C., Balsam, W., Adams, D., Mezger, K., and Andreae, M. O.: Geochemical and isotopic characterization of the Bodele Depression dust source and implications for transatlantic dust transport to the Amazon Basin, Earth Planet. Sci. Lett., 380, 112-123, 10.1016/j.epsl.2013.08.028, 2013.

Acker, J. G., and Leptoukh, G.: Online analysis enhances use of NASA Earth science data, Eos, Transactions American Geophysical Union, 88, 14-17, 10.1029/2007EO020003, 2007.

Andreae, M. O.: Aerosols before pollution, Science, 315, 50-51, 10.1126/science.1136529, 2007.

Andreae, M. O., Acevedo, O. C., Araùjo, A., Artaxo, P., Barbosa, C. G. G., Barbosa, H. M. J., Brito, J., Carbone, S., Chi, X., Cintra, B. B. L., da Silva, N. F., Dias, N. L., Dias-Júnior, C. Q., Ditas, F., Ditz, R., Godoi, A. F. L., Godoi, R. H. M., Heimann, M., Hoffmann, T., Kesselmeier, J., Könemann, T., Krüger, M. L., Lavric, J. V., Manzi, A. O., Moran-Zuloaga, D., Nölscher, A. C., Santos Nogueira, D., Piedade, M. T. F., Pöhlker, C., Pöschl, U., Rizzo, L. V., Ro, C. U., Ruckteschler, N., Sá, L. D. A., Sá, M. D. O., Sales, C. B., Santos, R. M. N. D., Saturno, J., Schöngart, J., Sörgel, M., de Souza, C. M., de Souza, R. A. F., Su, H., Targhetta, N., Tóta, J., Trebs, I., Trumbore, S., van Eijck, A., Walter, D., Wang, Z., Weber, B., Williams, J., Winderlich, J., Wittmann, F., Wolff, S., and Yáñez-Serrano, A. M.: The Amazon Tall Tower Observatory (ATTO): overview of pilot measurements on ecosystem ecology, meteorology, trace gases, and aerosols, Atmos. Chem. Phys., 15, 10723-10776, 10.5194/acp-15-10723-2015, 2015.

Andreae, M. O., Afchine, A., Albrecht, R., Holanda, B. A., Artaxo, P., Barbosa, H. M. J., Bormann, S., Cecchini, M. A., Costa, A., Dollner, M., Fütterer, D., Järvinen, E., Jurkat, T., Klimach, T., Könemann, T., Knote, C., Krämer, M., Krisna, T., Machado, L. A. T., Mertes, S., Minikin, A., Pöhlker, C., Pöhlker, M. L., Pöschl, U., Rosenfeld, D., Sauer, D., Schlager, H., Schnaiter, M., Schneider, J., Schulz, C., Spanu, A., Sperling, V. B., Voigt, C., Walser, A., Wang, J., Weinzierl, B., Wendisch, M., and Ziereis, H.: Aerosol characteristics and particle production in the upper troposphere over the Amazon Basin, Atmos. Chem. Phys. Discuss., 2017.

Andreae, M. O., Anderson, B. E., Blake, D. R., Bradshaw, J. D., Collins, J. E., Gregory, G. L., Sachse, G. W., and Shipham, M. C.: INFLUENCE OF PLUMES FROM BIOMASS BURNING ON ATMOSPHERIC CHEMISTRY OVER THE EQUATORIAL AND TROPICAL SOUTH-ATLANTIC DURING CITE-3, Journal of Geophysical Research-Atmospheres, 99, 12793-12808, 10.1029/94jd00263, 1994.

Andreae, M. O., Artaxo, P., Beck, V., Bela, M., Freitas, S., Gerbig, C., Longo, K., Munger, J. W., Wiedemann, K. T., and Wofsy, S. C.: Carbon monoxide and related trace gases and aerosols over the Amazon Basin during the wet and dry seasons, Atmospheric Chemistry and Physics, 12, 6041-6065, 10.5194/acp-12-6041-2012, 2012.

Andreae, M. O., Charlson, R. J., Bruynseels, F., Storms, H., Vangrieken, R., and Maenhaut, W.: Internal Mixture of Sea Salt, Silicates, and Excess Sulfate in Marine Aerosols, Science, 232, 1620-1623, 10.1126/science.232.4758.1620, 1986.

Andreae, M. O., and Rosenfeld, D.: Aerosol-cloud-precipitation interactions. Part 1. The nature and sources of cloud-active aerosols, Earth-Sci. Rev., 89, 13-41, 10.1016/j.earscirev.2008.03.001, 2008.

Andreae, M. O., Rosenfeld, D., Artaxo, P., Costa, A. A., Frank, G. P., Longo, K. M., and Silva-Dias, M. A. F.: Smoking rain clouds over the Amazon, Science, 303, 1337-1342, 10.1126/science.1092779, 2004.

Artaxo, P., Rizzo, L. V., Brito, J. F., Barbosa, H. M. J., Arana, A., Sena, E. T., Cirino, G. G., Bastos, W., Martin, S. T., and Andreae, M. O.: Atmospheric aerosols in Amazonia and land use change: from natural biogenic to biomass burning conditions, Faraday Discuss., 165, 203-235, 10.1039/c3fd00052d, 2013.

Atwood, S. A., Reid, J. S., Kreidenweis, S. M., Blake, D. R., Jonsson, H. H., Lagrosas, N. D., Xian, P., Reid, E. A., Sessions, W. R., and Simpas, J. B.: Size-resolved aerosol and cloud condensation nuclei (CCN) properties in the remote marine South China Sea – Part 1: Observations and source classification, Atmos. Chem. Phys., 17, 1105-1123, 10.5194/acp-17-1105-2017, 2017.

Baars, H., Ansmann, A., Althausen, D., Engelmann, R., Artaxo, P., Pauliquevis, T., and Souza, R.: Further evidence for significant smoke transport from Africa to Amazonia, Geophys. Res. Lett., 38, L20802, L20802

10.1029/2011gl049200, 2011.

Bony, S., Stevens, B., Frierson, D. M. W., Jakob, C., Kageyama, M., Pincus, R., Shepherd, T. G., Sherwood, S. C., Siebesma, A. P., Sobel, A. H., Watanabe, M., and Webb, M. J.: Clouds, circulation and climate sensitivity, Nature Geoscience, 8, 261-268, 10.1038/ngeo2398, 2015.

Braga, R. C., Rosenfeld, D., Weigel, R., Jurkat, T., Andreae, M. O., Wendisch, M., Pöhlker, M. L., Klimach, T., Pöschl, U., Pöhlker, C., Voigt, C., Mahnke, C., Borrmann, S., Albrecht, R. I., Molleker, S., Vila, D. A., Machado, L. A. T., and Artaxo, P.: Comparing parameterized versus measured microphysical properties of tropical convective cloud bases during the ACRIDICON–CHUVA campaign, Atmos. Chem. Phys., 17, 7365-7386, 10.5194/acp-17-7365-2017, 2017.

Bristow, C. S., Hudson-Edwards, K. A., and Chappell, A.: Fertilizing the Amazon and equatorial Atlantic with West African dust, Geophys. Res. Lett., 37, 10.1029/2010gl043486, 2010.

Carbone, S., Brito, J. F., Xu, L., Ng, N. L., Rizzo, L., Holanda, B. A., Wolff, S., Saturno, J., Chi, X., Souza, R. A. F., Pöhlker, M. L., Andreae, M. O., Pöhlker, C., Barbosa, H. M. J., and Artaxo, P.: Long-term chemical composition and source apportionment of submicron aerosol particles in the central Amazon basin (ATTO), Atmos. Chem. Phys., in prep., 2017.

5   Carslaw, K. S., Lee, L. A., Reddington, C. L., Pringle, K. J., Rap, A., Forster, P. M., Mann, G. W., Spracklen, D. V., Woodhouse, M. T., Regayre, L. A., and Pierce, J. R.: Large contribution of natural aerosols to uncertainty in indirect forcing, Nature, 503, 67-+, 10.1038/nature12674, 2013.

Cecchini, M. A., Machado, L. A. T., Andreae, M. O., Martin, S. T., Albrecht, R. I., Artaxo, P., Barbosa, H. M. J., Borrmann, S., Fütterer, D., Jurkat, T., Mahnke, C., Minikin, A., Molleker, S., Pöhlker, M. L., Pöschl, U., Rosenfeld, D., Voigt, C., Wenzierl, B., and Wendisch, M.: Sensitivities of Amazonian clouds to aerosols and updraft speed, Atmos. Chem. Phys., 17,
10   10037-10050, https://doi.org/10.5194/acp-17-10037-2017, 2017a.

Cecchini, M. A., Machado, L. A. T., Wendisch, M., Costa, A., Krämer, M., Andreae, M. O., Afchine, A., Albrecht, R. I., Artaxo, P., Borrmann, S., Fütterer, D., Klimach, T., Mahnke, C., Martin, S. T., Minikin, A., Molleker, S., Pardo, L. H., Pöhlker, C., Pöhlker, M. L., Pöschl, U., Rosenfeld, D., and Weinzierl, B.: Illustration of microphysical processes in Amazonian deep convective clouds in the Gamma phase space: Introduction and potential applications, Atmos. Chem. Phys.
15   Discuss., 2017, 1-49, 10.5194/acp-2017-185, 2017b.

Chen, Q., Farmer, D. K., Schneider, J., Zorn, S. R., Heald, C. L., Karl, T. G., Guenther, A., Allan, J. D., Robinson, N., Coe, H., Kimmel, J. R., Pauliquevis, T., Borrmann, S., Poschl, U., Andreae, M. O., Artaxo, P., Jimenez, J. L., and Martin, S. T.: Mass spectral characterization of submicron biogenic organic particles in the Amazon Basin, Geophys. Res. Lett., 36, L20806, L20806, 10.1029/2009gl039880, 2009.

20   Davidson, E. A., de Araujo, A. C., Artaxo, P., Balch, J. K., Brown, I. F., Bustamante, M. M. C., Coe, M. T., DeFries, R. S., Keller, M., Longo, M., Munger, J. W., Schroeder, W., Soares-Filho, B. S., Souza, C. M., Jr., and Wofsy, S. C.: The Amazon basin in transition, Nature, 481, 321-328, 10.1038/nature10717, 2012.

Draxler, R. R., and Hess, G. D.: An overview of the HYSPLIT_4 modelling system for trajectories, dispersion and deposition, Australian Meteorological Magazine, 47, 295-308, 1998.

25   Ekman, A. M. L., Krejci, R., Engstrom, A., Strom, J., de Reus, M., Williams, J., and Andreae, M. O.: Do organics contribute to small particle formation in the Amazonian upper troposphere?, Geophys. Res. Lett., 35, L17810, L17810, 10.1029/2008gl034970, 2008.

Engstrom, A., Ekman, A. M. L., Krejci, R., Strom, J., de Reus, M., and Wang, C.: Observational and modelling evidence of tropical deep convective clouds as a source of mid-tropospheric accumulation mode aerosols, Geophys. Res. Lett., 35,
30   L23813, 10.1029/2008gl035817, 2008.

Ervens, B.: Modeling the Processing of Aerosol and Trace Gases in Clouds and Fogs, Chemical Reviews, 115, 4157-4198, 10.1021/cr5005887, 2015.

Farmer, D. K., Cappa, C. D., and Kreidenweis, S. M.: Atmospheric Processes and Their Controlling Influence on Cloud Condensation Nuclei Activity, Chemical Reviews, 115, 4199-4217, 10.1021/cr5006292, 2015.

35   Fearnside, P. M.: Brazil's Cuiaba-Santarem (BR-163) Highway: The environmental cost of paving a soybean corridor through the amazon, Environmental Management, 39, 601-614, 10.1007/s00267-006-0149-2, 2007.

Fioletov, V. E., McLinden, C. A., Krotkov, N., Li, C., Joiner, J., Theys, N., Carn, S., and Moran, M. D.: A global catalogue of large SO2 sources and emissions derived from the Ozone Monitoring Instrument, Atmospheric Chemistry and Physics, 16, 11497-11519, 10.5194/acp-16-11497-2016, 2016.

40   Freitas, S. R., Longo, K. M., Diasb, M., Diasb, P. L. S., Chatfield, R., Prins, E., Artaxo, P., Grell, G. A., and Recuero, F. S.: Monitoring the transport of biomass burning emissions in South America, Environmental Fluid Mechanics, 5, 135-167, 10.1007/s10652-005-0243-7, 2005.

Freud, E., Rosenfeld, D., Andreae, M. O., Costa, A. A., and Artaxo, P.: Robust relations between CCN and the vertical evolution of cloud drop size distribution in deep convective clouds, Atmospheric Chemistry and Physics, 8, 1661-1675, 2008.

45   Fuzzi, S., Decesari, S., Facchini, M. C., Cavalli, F., Emblico, L., Mircea, M., Andreae, M. O., Trebs, I., Hoffer, A., Guyon, P., Artaxo, P., Rizzo, L. V., Lara, L. L., Pauliquevis, T., Maenhaut, W., Raes, N., Chi, X., Mayol-Bracero, O. L., Soto-Garcia, L. L., Claeys, M., Kourtchev, I., Rissler, J., Swietlicki, E., Tagliavini, E., Schkolnik, G., Falkovich, A. H., Rudich, Y., Fisch, G., and Gatti, L. V.: Overview of the inorganic and organic composition of size-segregated aerosol in Rondonia, Brazil, from the biomass-burning period to the onset of the wet season, Journal of Geophysical Research-Atmospheres, 112,
50   10.1029/2005jd006741, 2007.

Glaser, G., Wernli, H., Kerkweg, A., and Teubler, F.: The transatlantic dust transport from North Africa to the Americas-Its characteristics and source regions, Journal of Geophysical Research-Atmospheres, 120, 11231-11252, 10.1002/2015jd023792, 2015.

Goncalves, W. A., Machado, L. A. T., and Kirstetter, P. E.: Influence of biomass aerosol on precipitation over the Central
55   Amazon: an observational study, Atmospheric Chemistry and Physics, 15, 6789-6800, 10.5194/acp-15-6789-2015, 2015.

Gunthe, S. S., King, S. M., Rose, D., Chen, Q., Roldin, P., Farmer, D. K., Jimenez, J. L., Artaxo, P., Andreae, M. O., Martin, S. T., and Poschl, U.: Cloud condensation nuclei in pristine tropical rainforest air of Amazonia: size-resolved measurements and modeling of atmospheric aerosol composition and CCN activity, Atmospheric Chemistry and Physics, 9, 7551-7575, 2009.

5   Hamilton, D. S., Lee, L. A., Pringle, K. J., Reddington, C. L., Spracklen, D. V., and Carslaw, K. S.: Occurrence of pristine aerosol environments on a polluted planet, Proceedings of the National Academy of Sciences of the United States of America, 111, 18466-18471, 10.1073/pnas.1415440111, 2014.

Huffman, J. A., Sinha, B., Garland, R. M., Snee-Pollmann, A., Gunthe, S. S., Artaxo, P., Martin, S. T., Andreae, M. O., and Pöschl, U.: Biological aerosol particle concentrations and size distributions measured in pristine tropical rainforest air during
10   AMAZE-08, Atmos. Chem. Phys., 12, 25181-25236, 2012.

Janhaell, S., Andreae, M. O., and Poeschl, U.: Biomass burning aerosol emissions from vegetation fires: particle number and mass emission factors and size distributions, Atmospheric Chemistry and Physics, 10, 1427-1439, 2010.

Jimenez, J. L., Canagaratna, M. R., Donahue, N. M., Prevot, A. S. H., Zhang, Q., Kroll, J. H., DeCarlo, P. F., Allan, J. D., Coe, H., Ng, N. L., Aiken, A. C., Docherty, K. S., Ulbrich, I. M., Grieshop, A. P., Robinson, A. L., Duplissy, J., Smith, J. D.,
15   Wilson, K. R., Lanz, V. A., Hueglin, C., Sun, Y. L., Tian, J., Laaksonen, A., Raatikainen, T., Rautiainen, J., Vaattovaara, P., Ehn, M., Kulmala, M., Tomlinson, J. M., Collins, D. R., Cubison, M. J., Dunlea, E. J., Huffman, J. A., Onasch, T. B., Alfarra, M. R., Williams, P. I., Bower, K., Kondo, Y., Schneider, J., Drewnick, F., Borrmann, S., Weimer, S., Demerjian, K., Salcedo, D., Cottrell, L., Griffin, R., Takami, A., Miyoshi, T., Hatakeyama, S., Shimono, A., Sun, J. Y., Zhang, Y. M., Dzepina, K., Kimmel, J. R., Sueper, D., Jayne, J. T., Herndon, S. C., Trimborn, A. M., Williams, L. R., Wood, E. C., Middlebrook, A. M.,
20   Kolb, C. E., Baltensperger, U., and Worsnop, D. R.: Evolution of Organic Aerosols in the Atmosphere, Science, 326, 1525-1529, 10.1126/science.1180353, 2009.

Justice, C., Giglio, L., Roy, D., Boschetti, L., Csiszar, I., Davies, D., Korontzi, S., Schroeder, W., O'Neal, K., and Morisette, J.: MODIS-Derived Global Fire Products, in: Land Remote Sensing and Global Environmental Change, edited by: Ramachandran, B., Justice, C. O., and Abrams, M. J., Remote Sensing and Digital Image Processing, Springer New York,
25   661-679, 2011.

Kandler, K., Lieke, K., Benker, N., Emmel, C., Kuepper, M., Mueller-Ebert, D., Ebert, M., Scheuvens, D., Schladitz, A., Schuetz, L., and Weinbruch, S.: Electron microscopy of particles collected at Praia, Cape Verde, during the Saharan Mineral Dust Experiment: particle chemistry, shape, mixing state and complex refractive index, Tellus Series B-Chemical and Physical Meteorology, 63, 475-496, 10.1111/j.1600-0889.2011.00550.x, 2011.

30   King, M. D., Platnick, S., Menzel, W. P., Ackerman, S. A., and Hubanks, P. A.: Spatial and Temporal Distribution of Clouds Observed by MODIS Onboard the Terra and Aqua Satellites, Ieee Transactions on Geoscience and Remote Sensing, 51, 3826-3852, 10.1109/tgrs.2012.2227333, 2013.

Koren, I., Kaufman, Y. J., Remer, L. A., and Martins, J. V.: Measurement of the effect of Amazon smoke on inhibition of cloud formation, Science, 303, 1342-1345, 10.1126/science.1089424, 2004.

35   Krüger, M. L., Mertes, S., Klimach, T., Cheng, Y. F., Su, H., Schneider, J., Andreae, M. O., Pöschl, U., and Rose, D.: Assessment of cloud supersaturation by size-resolved aerosol particle and cloud condensation nuclei (CCN) measurements, Atmos. Meas. Tech., 7, 2615-2629, 10.5194/amt-7-2615-2014, 2014.

Kuhn, U., Ganzeveld, L., Thielmann, A., Dindorf, T., Schebeske, G., Welling, M., Sciare, J., Roberts, G., Meixner, F. X., Kesselmeier, J., Lelieveld, J., Kolle, O., Ciccioli, P., Lloyd, J., Trentmann, J., Artaxo, P., and Andreae, M. O.: Impact of
40   Manaus City on the Amazon Green Ocean atmosphere: ozone production, precursor sensitivity and aerosol load, Atmospheric Chemistry and Physics, 10, 9251-9282, 10.5194/acp-10-9251-2010, 2010.

Kulmala, M., Vehkamaki, H., Petaja, T., Dal Maso, M., Lauri, A., Kerminen, V. M., Birmili, W., and McMurry, P. H.: Formation and growth rates of ultrafine atmospheric particles: a review of observations, Journal of Aerosol Science, 35, 143-176, 10.1016/j.jaerosci.2003.10.003, 2004.

45   Lathem, T. L., Beyersdorf, A. J., Thornhill, K. L., Winstead, E. L., Cubison, M. J., Hecobian, A., Jimenez, J. L., Weber, R. J., Anderson, B. E., and Nenes, A.: Analysis of CCN activity of Arctic aerosol and Canadian biomass burning during summer 2008, Atmospheric Chemistry and Physics, 13, 2735-2756, 10.5194/acp-13-2735-2013, 2013.

Martin, S. T., Andreae, M. O., Althausen, D., Artaxo, P., Baars, H., Borrmann, S., Chen, Q., Farmer, D. K., Guenther, A., Gunthe, S. S., Jimenez, J. L., Karl, T., Longo, K., Manzi, A., Muller, T., Pauliquevis, T., Petters, M. D., Prenni, A. J., Poschl,
50   U., Rizzo, L. V., Schneider, J., Smith, J. N., Swietlicki, E., Tota, J., Wang, J., Wiedensohler, A., and Zorn, S. R.: An overview of the Amazonian Aerosol Characterization Experiment 2008 (AMAZE-08), Atmospheric Chemistry and Physics, 10, 11415-11438, 10.5194/acp-10-11415-2010, 2010a.

Martin, S. T., Andreae, M. O., Artaxo, P., Baumgardner, D., Chen, Q., Goldstein, A. H., Guenther, A., Heald, C. L., Mayol-Bracero, O. L., McMurry, P. H., Pauliquevis, T., Poschl, U., Prather, K. A., Roberts, G. C., Saleska, S. R., Dias, M. A. S.,
55   Spracklen, D. V., Swietlicki, E., and Trebs, I.: Sources and properties of Amazonian aerosol particles, Rev. Geophys., 48, RG2002, 10.1029/2008rg000280, 2010b.

Martin, S. T., Artaxo, P., Machado, L., Manzi, A. O., Souza, R. A. F., Schumacher, C., Wang, J., Biscaro, T., Brito, J., Calheiros, A., Jardine, K., Medeiros, A., Portela, B., Sá, S. S. d., Adachi, K., Aiken, A. C., Albrecht, R., Alexander, L.,

Andreae, M. O., Barbosa, H. M. J., Buseck, P., Chand, D., Comstock, J. M., Day, D. A., Dubey, M., Fan, J., Fast, J., Fisch, G., Fortner, E., Giangrande, S., Gilles, M., Goldstein, A. H., Guenther, A., Hubbe, J., Jensen, M., Jimenez, J. L., Keutsch, F. N., Kim, S., Kuang, C., Laskin, A., McKinney, K., Mei, F., Miller, M., Nascimento, R., Pauliquevis, T., Pekour, M., Peres, J., Petäjä, T., Pöhlker, C., Pöschl, U., Rizzo, L., Schmid, B., Shilling, J. E., Dias, M. A. S., Smith, J. N., Tomlinson, J. M., Tóta,
5   J., and Wendisch, M.: The Green Ocean Amazon Experiment (GoAmazon2014/5) Observes Pollution Affecting Gases, Aerosols, Clouds, and Rainfall over the Rain Forest, Bulletin of the American Meteorological Society, 0, null, 10.1175/bams-d-15-00221.1, 2016a.

Martin, S. T., Artaxo, P., Machado, L. A. T., Manzi, A. O., Souza, R. A. F., Schumacher, C., Wang, J., Andreae, M. O., Barbosa, H. M. J., Fan, J., Fisch, G., Goldstein, A. H., Guenther, A., Jimenez, J. L., Pöschl, U., Silva Dias, M. A., Smith, J.
10   N., and Wendisch, M.: Introduction: Observations and modeling of the Green Ocean Amazon (GoAmazon2014/5), Atmospheric Chemistry and Physics, 4785-4797, 10.5194/acp-16-4785-2016, 2016b.

Moran-Zuloaga, D., Ditas, F., Walter, D., Araùjo, A., Brito, J., Carbone, S., Chi, X., Hrabe de Angelis, I., Lavric, J. V., Ming, J., Pöhlker, M. L., Ruckteschler, N., Saturno, J., Wang, Y., Wang, Q., Weber, B., Wolff, S., Artaxo, P., Andreae, M. O., and Pöhlker, C.: Coarse mode aerosols in the Amazon rain forest – A multi-year study on the frequent advection of African dust
15   plumes Atmos. Chem. Phys., 2017.

Nepstad, D., McGrath, D., Alencar, A., Barros, A. C., Carvalho, G., Santilli, M., and Diaz, M. D. V.: Environment - Frontier governance in Amazonia, Science, 295, 629-+, 10.1126/science.1067053, 2002.

Ng, N. L., Herndon, S. C., Trimborn, A., Canagaratna, M. R., Croteau, P. L., Onasch, T. B., Sueper, D., Worsnop, D. R., Zhang, Q., Sun, Y. L., and Jayne, J. T.: An Aerosol Chemical Speciation Monitor (ACSM) for Routine Monitoring of the
20   Composition and Mass Concentrations of Ambient Aerosol, Aerosol Science and Technology, 45, 780-794, 10.1080/02786826.2011.560211, 2011.

Petzold, A., and Schonlinner, M.: Multi-angle absorption photometry - a new method for the measurement of aerosol light absorption and atmospheric black carbon, Journal of Aerosol Science, 35, 421-441, 10.1016/j.jaerosci.2003.09.005, 2004.

Pöhlker, C., Walter, D., Paulsen, H., Könemann, T., Moran-Zuloaga, D., Brito, J., Carbone, S., Degrendele, C., Després, V.
25   R., Ditas, F., Holanda, B. A., Lammel, G., Lavrič, J. V., Jing, M., Pickersgill, D., Pöhlker, M. L., Rodríguez-Caballero, E., Ruckteschler, N., Saturno, J., Sörgel, M., Wang, Q., Weber, B., Wolff, S., Artaxo, P., Pöschl, U., and Andreae, M. O.: Systematic backward trajectory and land cover analyses within the footprint of the remote ATTO site in the central Amazon Basin Atmos. Chem. Phys., to be submitted, 2017.

Pöhlker, M. L., Pöhlker, C., Klimach, T., Hrabe de Angelis, I., Barbosa, H. M. J., Brito, J., Carbone, S., Cheng, Y., Chi, X.,
30   Ditas, F., Ditz, R., Gunthe, S. S., Kesselmeier, J., Könemann, T., Lavrič, J. V., Martin, S. T., Moran-Zuloaga, D., Rose, D., Saturno, J., Su, H., Thalman, R., Walter, D., Wang, J., Wolff, S., Artaxo, P., Andreae, M. O., and Pöschl, U.: Long-term observations of cloud condensation nuclei in the Amazon rain forest – Part 1: Aerosol size distribution, hygroscopicity, and new model parameterizations for CCN prediction, Atmos. Chem. Phys., 16, 15709-15740, 10.5194/acp-2016-519, 2016.

Pöschl, U., Martin, S. T., Sinha, B., Chen, Q., Gunthe, S. S., Huffman, J. A., Borrmann, S., Farmer, D. K., Garland, R. M.,
35   Helas, G., Jimenez, J. L., King, S. M., Manzi, A., Mikhailov, E., Pauliquevis, T., Petters, M. D., Prenni, A. J., Roldin, P., Rose, D., Schneider, J., Su, H., Zorn, S. R., Artaxo, P., and Andreae, M. O.: Rainforest Aerosols as Biogenic Nuclei of Clouds and Precipitation in the Amazon, Science, 329, 1513-1516, 10.1126/science.1191056, 2010.

Reutter, P., Su, H., Trentmann, J., Simmel, M., Rose, D., Gunthe, S. S., Wernli, H., Andreae, M. O., and Poschl, U.: Aerosol-and updraft-limited regimes of cloud droplet formation: influence of particle number, size and hygroscopicity on the
40   activation of cloud condensation nuclei (CCN), Atmospheric Chemistry and Physics, 9, 7067-7080, 2009.

Rissler, J., Swietlicki, E., Zhou, J., Roberts, G., Andreae, M. O., Gatti, L. V., and Artaxo, P.: Physical properties of the sub-micrometer aerosol over the Amazon rain forest during the wet-to-dry season transition - comparison of modeled and measured CCN concentrations, Atmospheric Chemistry and Physics, 4, 2119-2143, 2004.

Rizzolo, J. A., Barbosa, C. G. G., Borillo, G. C., Godoi, A. F. L., Souza, R. A. F., Andreoli, R. V., Manzi, A. O., Sá, M. O.,
45   Alves, E. G., Pöhlker, C., Angelis, I. H., Ditas, F., Saturno, J., Moran-Zuloaga, D., Rizzo, L. V., Rosário, N. E., Pauliquevis, T., Yamamoto, C. I., Andreae, M. O., Taylor, P. E., and Godoi, R. H. M.: Mineral nutrients in Saharan dust and their potential impact on Amazon rainforest ecology, Atmos. Chem. Phys. Discuss., 2016, 1-43, 10.5194/acp-2016-557, 2016.

Roberts, G. C., Artaxo, P., Zhou, J. C., Swietlicki, E., and Andreae, M. O.: Sensitivity of CCN spectra on chemical and physical properties of aerosol: A case study from the Amazon Basin, Journal of Geophysical Research-Atmospheres, 107,
50   10.1029/2001jd000583, 2002.

Roberts, G. C., Nenes, A., Seinfeld, J. H., and Andreae, M. O.: Impact of biomass burning on cloud properties in the Amazon Basin, Journal of Geophysical Research-Atmospheres, 108, 10.1029/2001jd000985, 2003.

Roberts, M. C., Andreae, M. O., Zhou, J. C., and Artaxo, P.: Cloud condensation nuclei in the Amazon Basin: "Marine" conditions over a continent?, Geophys. Res. Lett., 28, 2807-2810, 2001.

55   Rosario, N. E., Longo, K. M., Freitas, S. R., Yamasoe, M. A., and Fonseca, R. M.: Modeling the South American regional smoke plume: aerosol optical depth variability and surface shortwave flux perturbation, Atmospheric Chemistry and Physics, 13, 2923-2938, 10.5194/acp-13-2923-2013, 2013.

Rose, D., Gunthe, S. S., Mikhailov, E., Frank, G. P., Dusek, U., Andreae, M. O., and Poeschl, U.: Calibration and measurement uncertainties of a continuous-flow cloud condensation nuclei counter (DMT-CCNC): CCN activation of ammonium sulfate and sodium chloride aerosol particles in theory and experiment, Atmospheric Chemistry and Physics, 8, 1153-1179, 2008.

Rosenfeld, D., Andreae, M. O., Asmi, A., Chin, M., de Leeuw, G., Donovan, D. P., Kahn, R., Kinne, S., Kivekas, N., Kulmala, M., Lau, W., Schmidt, K. S., Suni, T., Wagner, T., Wild, M., and Quaas, J.: Global observations of aerosol-cloud-precipitation-climate interactions, Rev. Geophys., 52, 750-808, 10.1002/2013rg000441, 2014.

Rosenfeld, D., Lohmann, U., Raga, G. B., O'Dowd, C. D., Kulmala, M., Fuzzi, S., Reissell, A., and Andreae, M. O.: Flood or drought: How do aerosols affect precipitation?, Science, 321, 1309-1313, 10.1126/science.1160606, 2008.

Rosenfeld, D., Zheng, Y., Hashimshoni, E., Pöhlker, M. L., Jefferson, A., Pöhlker, C., Yu, X., Zhu, Y., Liu, G., Yue, Z., Fischman, B., Li, Z., Giguzin, D., Goren, T., Artaxo, P., Barbosa, H. M. J., Pöschl, U., and Andreae, M. O.: Satellite retrieval of cloud condensation nuclei concentrations by using clouds as CCN chambers, Proceedings of the National Academy of Sciences, 113, 5828-5834, 10.1073/pnas.1514044113, 2016a.

Rosenfeld, D., Zheng, Y. T., Hashimshoni, E., Pohlker, M. L., Jefferson, A., Pohlker, C., Yu, X., Zhu, Y. N., Liu, G. H., Yue, Z. G., Fischman, B., Li, Z. Q., Giguzin, D., Goren, T., Artaxo, P., Barbosa, H. M. J., Poschl, U., and Andreae, M. O.: Satellite retrieval of cloud condensation nuclei concentrations by using clouds as CCN chambers, Proceedings of the National Academy of Sciences of the United States of America, 113, 5828-5834, 10.1073/pnas.1514044113, 2016b.

Saturno, J., Ditas, F., Pöhlker, M. L., Carbone, S., Brito, J., Holanda, B. A., Hrabě de Angelis, I., Morán-Zuloaga, D., Walter, D., Artaxo, P., Pöschl, U., Andreae, M. O., and Pöhlker, C.: African volcanic sulfur emissions as a contributor to atmospheric sulfate aerosol over the Amazon rain forest, Atmos. Chem. Phys., to be submitted, 2017a.

Saturno, J., Pöhlker, C., Massabò, D., Brito, J., Carbone, S., Cheng, Y., Chi, X., Ditas, F., Hrabě de Angelis, I., Morán-Zuloaga, D., Pöhlker, M. L., Rizzo, L. V., Walter, D., Wang, Q., Artaxo, P., Prati, P., and Andreae, M. O.: Comparison of different Aethalometer correction schemes and a reference multi-wavelength absorption technique for ambient aerosol data, Atmospheric Measurement Techniques, in prep., 2016.

Saturno, J., Pöhlker, C., Wang, Q., Ditas, F., Morán-Zuloaga, D., Brito, J., Carbone, S., Cheng, Y., Chi, X., Hoffmann, T., Holanda, B. A., Hrabe de Angelis, I., Könemann, T., Lavric, J. V., Jing, M., Pöhlker, M. L., Rizzo, L. V., Walter, D., Wolff, S., Artaxo, P., Pöschl, U., and Andreae, M. O.: Aerosol optical properties over central Amazonia: Long-term measurements at the ATTO site Atmos. Chem. Phys., to be submitted, 2017b.

Seinfeld, J. H., Bretherton, C., Carslaw, K. S., Coe, H., DeMott, P. J., Dunlea, E. J., Feingold, G., Ghan, S., Guenther, A. B., Kahn, R., Kraucunas, I., Kreidenweis, S. M., Molina, M. J., Nenes, A., Penner, J. E., Prather, K. A., Ramanathan, V., Ramaswamy, V., Rasch, P. J., Ravishankara, A. R., Rosenfeld, D., Stephens, G., and Wood, R.: Improving our fundamental understanding of the role of aerosol-cloud interactions in the climate system, Proceedings of the National Academy of Sciences of the United States of America, 113, 5781-5790, 10.1073/pnas.1514043113, 2016.

Stevens, B., and Feingold, G.: Untangling aerosol effects on clouds and precipitation in a buffered system, Nature, 461, 607-613, 10.1038/nature08281, 2009.

Swap, R., Garstang, M., Greco, S., Talbot, R., and Kallberg, P.: SAHARAN DUST IN THE AMAZON BASIN, Tellus Series B-Chemical and Physical Meteorology, 44, 133-149, 10.1034/j.1600-0889.1992.t01-1-00005.x, 1992.

Talbot, R. W., Andreae, M. O., Berresheim, H., Artaxo, P., Garstang, M., Harriss, R. C., Beecher, K. M., and Li, S. M.: AEROSOL CHEMISTRY DURING THE WET SEASON IN CENTRAL AMAZONIA - THE INFLUENCE OF LONG-RANGE TRANSPORT, Journal of Geophysical Research-Atmospheres, 95, 16955-16969, 10.1029/JD095iD10p16955, 1990.

Tao, W. K., Chen, J. P., Li, Z. Q., Wang, C., and Zhang, C. D.: IMPACT OF AEROSOLS ON CONVECTIVE CLOUDS AND PRECIPITATION, Rev. Geophys., 50, 10.1029/2011rg000369, 2012.

Thalman, R., de Sá, S. S., Palm, B. B., Barbosa, H. M. J., Pöhlker, M. L., Alexander, M. L., Brito, J., Carbone, S., Castillo, P., Day, D. A., Kuang, C., Manzi, A., Ng, N. L., Sedlacek III, A. J., Souza, R., Springston, S., Watson, T., Pöhlker, C., Pöschl, U., Andreae, M. O., Artaxo, P., Jimenez, J. L., Martin, S. T., and Wang, J.: CCN activity and organic hygroscopicity of aerosols downwind of an urban region in central Amazonia: Seasonal and diel variations and impact of anthropogenic emissions, Atmos. Chem. Phys., accepted, 2017.

Wang, J., Krejci, R., Giangrande, S., Kuang, C., Barbosa, H. M. J., Brito, J., Carbone, S., Chi, X., Comstock, J., Ditas, F., Lavric, J., Manninen, H. E., Mei, F., Moran-Zuloaga, D., Pöhlker, C., Pöhlker, M. L., Saturno, J., Schmid, B., Souza, R. A. F., Springston, S. R., Tomlinson, J. M., Toto, T., Walter, D., Wimmer, D., Smith, J. N., Kulmala, M., Machado, L. A. T., Artaxo, P., Andreae, M. O., Petäjä, T., and Martin, S. T.: Amazon boundary layer aerosol concentration sustained by vertical transport during rainfall, Nature, 539, 416-419, 10.1038/nature19819, 2016.

Wang, X., Zhang, L., and Moran, M. D.: Uncertainty assessment of current size-resolved parameterizations for below-cloud particle scavenging by rain, Atmos. Chem. Phys., 10, 5685-5705, 10.5194/acp-10-5685-2010, 2010.

Wendisch, M., Pöschl, U., Andreae, M. O., Machado, L. A. T., Albrecht, R., Schlager, H., Rosenfeld, D., Martin, S. T., Abdelmonem, A., Afchine, A., Araùjo, A. C., Artaxo, P., Aufmhoff, H., Barbosa, H. M. J., Borrmann, S., Braga, R.,

5 Buchholz, B., Cecchini, M. A., Costa, A., Curtius, J., Dollner, M., Dorf, M., Dreiling, V., Ebert, V., Ehrlich, A., Ewald, F., Fisch, G., Fix, A., Frank, F., Fütterer, D., Heckl, C., Heidelberg, F., Hüneke, T., Jäkel, E., Järvinen, E., Jurkat, T., Kanter, S., Kästner, U., Kenntner, M., Kesselmeier, J., Klimach, T., Knecht, M., Kohl, R., Kölling, T., Krämer, M., Krüger, M., Krisna, T. C., Lavric, J. V., Longo, K., Mahnke, C., Manzi, A. O., Mayer, B., Mertes, S., Minikin, A., Molleker, S., Münch, S., Nillius, B., Pfeilsticker, K., Pöhlker, C., Roiger, A., Rose, D., Rosenow, D., Sauer, D., Schnaiter, M., Schneider, J., Schulz, C., Souza, R. A. F. d., Spanu, A., Stock, P., Vila, D., Voigt, C., Walser, A., Walter, D., Weigel, R., Weinzierl, B., Werner, F., Yamasoe, M. A., Ziereis, H., Zinner, T., and Zöger, M.: ACRIDICON–CHUVA Campaign: Studying Tropical Deep Convective Clouds and Precipitation over Amazonia Using the New German Research Aircraft HALO, Bulletin of the American Meteorological Society, 97, 1885-1908, 10.1175/bams-d-14-00255.1, 2016.

10 Winderlich, J., Chen, H., Gerbig, C., Seifert, T., Kolle, O., Lavrič, J. V., Kaiser, C., Höfer, A., and Heimann, M.: Continuous low-maintenance CO2/CH4/H2O measurements at the Zotino Tall Tower Observatory (ZOTTO) in Central Siberia, Atmos. Meas. Tech., 3, 1113-1128, 10.5194/amt-3-1113-2010, 2010.

Yanez-Serrano, A. M., Noelscher, A. C., Williams, J., Wolff, S., Alves, E., Martins, G. A., Bourtsoukidis, E., Brito, J., Jardine, K., Artaxo, P., and Kesselmeier, J.: Diel and seasonal changes of biogenic volatile organic compounds within and
15 above an Amazonian rainforest, Atmospheric Chemistry and Physics, 15, 3359-3378, 10.5194/acp-15-3359-2015, 2015.

Yu, H. B., Chin, M., Yuan, T. L., Bian, H. S., Remer, L. A., Prospero, J. M., Omar, A., Winker, D., Yang, Y. K., Zhang, Y., Zhang, Z. B., and Zhao, C.: The fertilizing role of African dust in the Amazon rainforest: A first multiyear assessment based on data from Cloud-Aerosol Lidar and Infrared Pathfinder Satellite Observations, Geophys. Res. Lett., 42, 1984-1991, 10.1002/2015gl063040, 2015.

20 Zhou, J., Swietlicki, E., Hansson, H. C., and Artaxo, P.: Submicrometer aerosol particle size distribution and hygroscopic growth measured in the Amazon rain forest during the wet season, J. Geophys. Res., 107, 8055, 10.1029/2000jd000203, 2002.

Zikova, N., and Zdimal, V.: Precipitation scavenging of aerosol particles at a rural site in the Czech Republic, Tellus Series B-Chemical and Physical Meteorology, 68, 10.3402/tellusb.v68.27343, 2016.

Table A1. List of frequently used symbols.

Symbol	Quantity and Unit
a_{mode} (mode =1, 2)	prefactor of single- and double erf fits
D	mobility equivalent particle diameter, nm
$D_a(S)$	midpoint activation diameter determined from CCN activation curve, nm
D_{Ait}	position of Aitken mode maximum, nm
D_{Acc}	position of accumulation mode maximum, nm
D_H	position of Hoppel minimum, nm
D_{cut}	cut-off diameter of aerosol impactor, nm
κ	hygroscopicity parameter
$\kappa(S,D_a)$	hygroscopicity parameter determined from CCN activation curve
κ_{Acc}	mean hygroscopicity parameter for accumulation mode particles
κ_{Ait}	mean hygroscopicity parameter for Aitken mode particles
κ_p	predicted hygroscopicity parameter based on ACSM results
$MAF(S)$	maximum activated fraction determined by CCN activation curve
M_{Bce}	mass concentration of BC_e, µg m^{-3}
$M_{Bce}{}^*$	threshold M_{BCe} level for definition of near-pristine periods, µg m^{-3}
M_{Org}	ACSM-derived organic mass concentration, µg m^{-3}
M_{NO3}	ACSM-derived nitrate mass concentration, µg m^{-3}
M_{NH4}	ACSM-derived ammonium mass concentration, µg m^{-3}
M_{SO4}	ACSM-derived sulfate mass concentration, µg m^{-3}
M_{Cl}	ACSM-derived chloride mass concentration, µg m^{-3}
N	number of data points
$N_{CCN}(S)$	CCN number concentration at a certain S, cm^{-3}
$N_{CCN}(S,D)$	CCN number concentration at a certain S and D, cm^{-3}
$N_{CCN}(S) / N_{CN,10}$	CCN efficiency
$N_{CN,Dcut}$	CN number concentration ($>D_{cut}$), cm^{-3}
$N_{CN,10}$	CN number concentration (>10 nm), cm^{-3}
$N_{CN,Acc}$	CN number concentration for accumulation mode particles, cm^{-3}
$N_{CN,Ait}$	CN number concentration for Aitken mode paticles, cm^{-3}
N_d	Cloud droplet number concentration, cm^{-3}
N_{db}	Cloud droplet number concentration at cloud base, cm^{-3}
P_{ATTO}	precipitation rate at ATTO, mm h^{-1}
P_{BT}	cumulative precipitation from HYSPLIT BTs, mm h^{-1}
P_{TRMM}	precipitation from TRMM satellite mission, mm h^{-1}
r_e	cloud droplet effective radius, µm
S	water vapor supersaturation, %
$S_{cloud}(D_H,\kappa)$	average peak supersaturation in cloud, %
S_{mode} (mode =1, 2)	midpoint activation supersaturation determined from CCN efficiency spectra, %
std	standard deviation
SW_{in}	incoming short-wave radiation, W m^{-2}
θ_e	equivalent potential temperature, K
U	wind speed, m s^{-1}
v_1	offset of single- and double erf fits
w	updraft velocity, m s^{-1}
w_b	updraft velocity at cloud base, m s^{-1}
w_{mode} (mode =1, 2)	width of CCN efficiency spectra
σ	width of log-normal fit in Aitken and accumulation mode fitting
σ_{ap}	aerosol absorption coefficient, Mm^{-1}
x_0	position of log-normal fit in Aitken and accumulation mode fitting, nm

Table A2. List of frequently used acronyms.

Acronym	Description
ACSM	aerosol chemical speciation monitor
ATTO	Amazon tall tower observatory
BB	biomass burning
BC	black carbon
BC_e	equivalent black carbon
BL	boundary layer
BT	backward trajectory
BVOC	biogenic volatile organic compound
CCN	cloud condensation nuclei
CCNC	cloud condensation nuclei counter
CPC	condensation particle counter
CS	case study
DSD	droplet size ditribution
erf	Gaussian error function
FIRMS	fire information for resource management system
GDAS	global data assimilation system
GoAmazon2014/5	green ocean Amazon 2014/5
HYSPLIT	hybrid single particle Lagrangian integrated trajectory model
IOP	intensive observation period
lpm	liters per minute
LRT	long-range transport
ITCZ	intertropical convergence zone
MAAP	multi-angle absorption photometer
MAC	mass absorption coefficient
MODIS	moderate resolution imaging spectroradiometer
NOAA	national oceanic and atmospheric administration
NP	near-pristine
NASA	National Aeronautics and Space Administration
NPF	new particle formation
OA	organic aerosol
PBAP	primary biological aerosol particles
rBC	refractory black carbon
RH	relative humidity
ROI_{ATTO}	region of interest, covering ATTO region
SE	standard error
SMPS	scanning mobility particle counter
SOA	secondary organic aerosol
SP2	single particle soot photometer
UT	upper troposphere
UTC	coordinated universal time

Table 1. Overview of case study names and time frames for detailed aerosol and CCN analysis. Note that time frames of different length were averaged for aerosol and CCN data products (i.e., size distributions, composition, CCN key parameters) depending on data availability.

Case study conditions and episodes		Time frames [UTC]	Specific remarks
near-pristine (NP)	all available NP periods	defined in Sect. 2.3	- For $N_{CN}(D)$, $N_{CCN}(S,D)$, $\kappa(S,D)$, CCN efficiency spectra (Fig. 6a and b): all available NP episodes within CCN measurement period (Mar 2014-Feb 2015) averaged.
	NP1	24 Apr 06:00 - 29 April 10:00 2014	- Episodes NP1, NP2, NP3 for detailed illustration of specific conditions in Fig. 5.
	NP2	04 May 23:00 - 08 May 10:00 2014	- For ACSM results (Table 2): all NP episodes within time frame 01 Aug 2014 to 30 Sep 2014 averaged.
	NP3	16 May 06:00 - 17 May 16:00 2014	
long-range transport (LRT)	LRT1	28 Mar 11:00 - 01 Apr 09:00 2014	- For $N_{CN}(D)$, $N_{CCN}(S,D)$, $\kappa(S,D)$, CCN efficiency spectra (Fig. 6c and d): LRT3 time frame averaged.
	LRT2	03 Apr 12:00 - 05 Apr 18:00 2014	- Episodes LRT1, LRT2, LRT3 highlighted in Fig. 2. LRT3 for detailed illustration of specific conditions in Fig. 7.
	LRT3	08 Apr 22:00 - 13 Apr 13:00 2014	- For ACSM results (Table 2): all LRT episodes within time frame 01 Aug 2014 to 30 Sep 2016 averaged.
	all available LRT episodes	see Moran-Zuloaga et al. (2017)	
biomass burning (BB)	BB	17 Aug 00:00 - 23 Aug 00:00 2014	- BB time frame averaged for: $N_{CN}(D)$, $N_{CCN}(S,D)$, $\kappa(S,D)$, CCN efficiency spectrum (Fig. 6e and f) and ACSM results (Table 2).
			- BB for detailed illustration of specific conditions in Fig. 8.
mixed pollution (MixPol)	low κ	Entire period: 22 Sep 00:40 - 01 Oct 03:30 2014 (for details refer to Fig. 9)	- Subcategories low κ and high κ during MixPol episode averaged independently for: $N_{CN}(D)$, $N_{CCN}(S,D)$, $\kappa(S,D)$, CCN efficiency spectra in (Fig. 6g, h and i), and ACSM averages (Table 2).
	high κ		- MixPol for detailed illustration of specific conditions in Fig. 9.

Table 2. Properties (position x_0, integral number concentration N_{CN}, width σ) of Aitken and accumulation modes from single or double log-normal fit (compare R^2) of the total particle size distribution. Values are given as means of the case study periods, whereas corresponding seasonally averaged results can be found in the part 1 study. The errors represent the uncertainty of the fit parameters. No meaningful double log-normal fit was obtained for the monomodal *MixPol* case – thus, a single log-normal fit was conducted to describe the properties of the main peak. For the case studies *NP* and *LRT* with a clearly resolved bimodal size distribution, values for the position of the Hoppel minimum D_H as well as estimated average peak supersaturation in cloud $S_{cloud}(D_H, \kappa)$ are listed. The errors in $S_{cloud}(D_H, \kappa)$ are the experimentally derived error in S.

Time period	Mode or size range	N_{CN} [cm^{-3}]	κ	x_0 [nm]	σ	R^2	D_H [nm]	$S_{cloud}(D_H,\kappa)$ [%]
Case study: near-pristine (*NP*)	Aitken	203 ± 6	0.12 ± 0.01	67 ± 1	0.60 ± 0.01	0.99	122 ± 2	0.20 ± 0.01
	accumulation	65 ± 4	0.18 ± 0.02	171 ± 2	0.34 ± 0.02			
Case study: long-range transport (*LRT*)	Aitken	120 ± 10	0.18 ± 0.02	77 ± 2	0.58 ± 0.03	0.99	109 ± 2	0.18 ± 0.01
	accumulation	300 ± 6	0.34 ± 0.04	178 ± 2	0.52 ± 0.01			
Case study: biomass burning (*BB*)	Aitken	140 ± 29	0.14 ± 0.01	70 ± 1	0.20 [a]	0.99	--	--
	accumulation	3439 ± 39	0.17 ± 0.02	167 ± 1	0.58 ± 0.01			
Case study: mixed pollution (*MixPol*) *high κ*	< 100 nm	--	0.14 ± 0.01	--	--	0.99	--	--
	> 100 nm	1272 ± 27	0.22 ± 0.03	135 ± 5	0.85 ± 0.01			
low κ	< 150 nm	--	0.10 ± 0.01	--	--	0.99	--	--
	> 150 nm	2764 ± 84	0.20 ± 0.04	113 ± 1	0.81 ± 0.01			

[a] Width of Aitken mode in double log-normal fit of BB case was predefined.

Table 3. Aerosol chemical composition from ACSM measurements at ATTO, showing characteristic differences between case studies as well as seasonal conditions (for details see Carbone et al., 2017). ACSM data was available for time period from 01 Aug 2014 to 30 Sep 2016 and the averaged values are shown here as mean ± std. Information on averaged time frames for the individual case studies can be found in Table 1. The shown ACSM 3σ detection limits for 30 min averaging time were obtained from Ng et al. (2011). Note that M_{NH4} ranged below the instruments detection limit in certain cases, which makes the corresponding results unreliable. Predicted average aerosol hygroscopicity parameter, κ_p, was calculated according to Gunthe et al. (2009) and is shown as mean ± standard error. The $\kappa(0.10\ \%)$ results are shown with the experimentally derived error.

| Time period | Mass concentrations $M_{species}$ [µg m^{-3}] & (Mass fraction [%]) | | | | | OA/SO_4^{2-} | κ_p | $\kappa(0.10\ \%)$ [b] |
	OA	NO$_3^-$	NH$_4^+$	SO$_4^{2-}$	Cl			
Case study: near-pristine (NP)	0.64 ± 0.56	0.03 ± 0.03	0.18 ± 0.19 [a]	0.04 ± 0.03	0.01 ± 0.01	~ 46	0.16 ± 0.05 *	0.19 ± 0.05
	(89)*	(4)*	(--)*	(6)*	(1)*			
Case study: long-range transport (LRT)	1.81 ± 2.63	0.08 ± 0.09	0.30 ± 0.37	0.25 ± 0.19	0.04 ± 0.05	~ 24	0.24 ± 0.16	0.35 ± 0.04
	(73)	(3)	(12)	(10)	(2)			
Case study: biomass burning (BB)	19.10 ± 6.65	0.50 ± 0.19	0.54 ± 0.25	0.79 ± 0.21	0.03 ± 0.02	~ 24	0.14 ± 0.02	0.18 ± 0.01
	(91)	(2)	(3)	(4)	(0)			
Case study: mixed pollution high κ	5.48 ± 1.07	0.22 ± 0.08	0.54 ± 0.25	1.76 ± 0.62	0.03 ± 0.02	~ 3	0.26 ± 0.04	0.26 ± 0.05
	(68)	(3)	(7)	(22)	(0)			
(MixPol) low κ	8.08 ± 1.34	0.36 ± 0.21	0.69 ± 0.26	2.05 ± 0.60	0.03 ± 0.01	~ 4	0.23 ± 0.03	0.24 ± 0.02
	(72)	(3)	(6)	(18)	(0)			
Wet season (Feb-May) [b]	1.02 ± 0.75	0.05 ± 0.06	0.20 ± 0.23 [a]	0.14 ± 0.18	0.02 ± 0.03	~ 23	0.19 ± 0.08 *	0.21 ± 0.05
	(83)*	(4)*	(--)*	(11)*	(2)*			
Transition periods (Jun/Jul & Dec/Jan)	3.16 ± 4.11	0.11 ± 0.12	0.13 ± 0.29 [a]	0.30 ± 0.31	0.02 ± 0.03	~ 21	0.16 ± 0.08 *	0.24 ± 0.05
	(88)*	(3)*	(--)*	(8)*	(1)*			
Dry season (Aug-Nov)	5.86 ± 5.46	0.19 ± 0.15	0.33 ± 0.24	0.64 ± 0.38	0.02 ± 0.03	~ 11	0.18 ± 0.07	0.21 ± 0.04
	(83)	(3)	(5)	(9)	(0)			
ACSM 3σ detection limits	0.148	0.012	0.284	0.024	0.011	--	--	--

[a] Here, measured M_{NH4} ranged below the ACSM detection limit and the shown values are questionable. For NP case study as well as averages of wet season and transition periods, mass factions and κ_p were calculated by omitting M_{NH4} as outlined in Sect. 2.1. The corresponding results are marked by *.

[b] The entirely averaged wet season includes NP and LRT conditions and, thus, concentrations represent an intermediate state of the NP and LRT cases.

Table 4. Error function (erf) fit parameters describing CCN efficiency spectra $N_{CCN}(S)/N_{CN,10}$ vs. S as model input data representing case studies as defined in this part 2 paper (upper part of table). For comparison, the erf fit parameters, presenting the seasonal averages from the companion part 1 paper (M. Pöhlker et al. 2016) are shown in the lower part of the table. A reference concentration of $N_{CN,10}$ has been used in all cases. Corresponding formulas can be found in Sect. 2.2.

Time period		N_{CN} [cm^{-3}]	erf fit	mode	y_{mode}	a_{mode}	S_{mode} [%]	w_{mode}	R^2	comment
Case study: near-pristine (NP)		271 ± 100	single	1	0.5	0.5	0.47 ± 0.01	1.69 ± 0.06	0.99	
			double	1	0.5	0.10 ± 0.03	0.11 ± 0.01	0.46 ± 0.25	0.99	
				2	-	0.40 ± 0.03	0.65 ± 0.06	1.18 ± 0.14		
Case study: long-range transport (LRT)		438 ± 96	single	1	0.5	0.5	0.09 ± 0.01	1.99 ± 0.16	0.96	fit parameters for CCN efficiency spectra in case studies as defined in the present **part 2** study
Case study: biomass burning (BB)		3200 ± 1039	single	1	0.5	0.5	0.15 ± 0.01	1.16 ± 0.13	0.96	
				1	0.43 ± 0.1	0.5	0.13 ± 0.01	0.94 ± 0.05	0.99	
Case study: mixed pollution	high κ	1277 ± 267	single	1	0.5	0.5	0.16 ± 0.01	1.70 ± 0.08	0.99	
(MixPol)	low κ	2776 ± 648	single	1	0.5	0.5	0.28 ± 0.01	1.60 ± 0.04	0.99	
seasonal average: wet		340 ± 139	single	1	0.5	0.5	0.35 ± 0.01	1.80 ± 0.06	0.99	fit parameters for seasonally averaged CCN efficiency spectra taken from **part 1** study (M. Pöhlker et al. 2016) for comparison
seasonal average: LRT		438 ± 244	single	1	0.5	0.5	0.22 ± 0.01	2.39 ± 0.10	0.98	
seasonal average: trans		1074 ± 385	single	1	0.5	0.5	0.28 ± 0.01	1.70 ± 0.05	0.99	
seasonal average: dry		1511 ± 785	single	1	0.5	0.5	0.18 ± 0.01	1.57 ± 0.11	0.98	
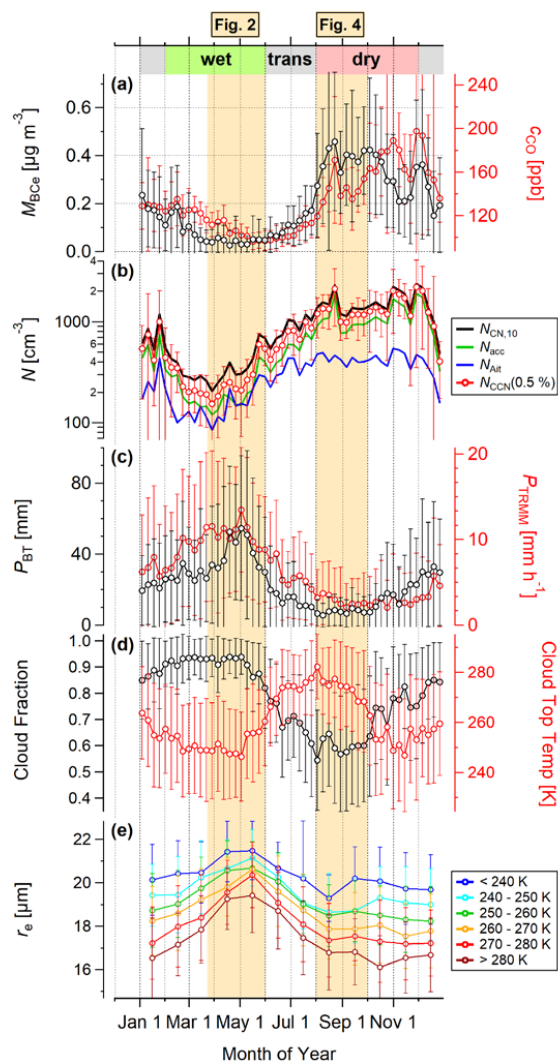
Figure 1. Seasonal cycle of selected trace gas, aerosol, and cloud microphysical parameters. **(a) Pollution tracers** M_{BCe}
and c_{CO}. **(b) Total aerosol number concentration** $N_{CN,10}$. **(c) Precipitation products** P_{BT}, **representing cumulative precip-**
itation along BT tracks, and P_{TRMM}, **representing TRMM-derived precipitation within the** ROI_{ATTO} **as defined in Fig.**
S1. (d) Satellite-derived cloud fraction and cloud top temperature within the ROI_{ATTO}. **(e). Satellite-derived cloud drop-**
let effective radius r_e **within the** ROI_{ATTO}. **For a detailed characterization of the land use and recent land use change in**
the ATTO site footprint, including the ROI_{ATTO}, **we refer the reader to a recent study on this topic (C. Pöhlker et al.,**
2017). Data in (a) to (d) is shown as weekly averages. Data in (e) is shown as monthly averages. Error bars represent
one standard deviation. Vertical orange shading represents 2-month time frames of representative clean and polluted
conditions as shown in detail in Fig. 2 and 4.
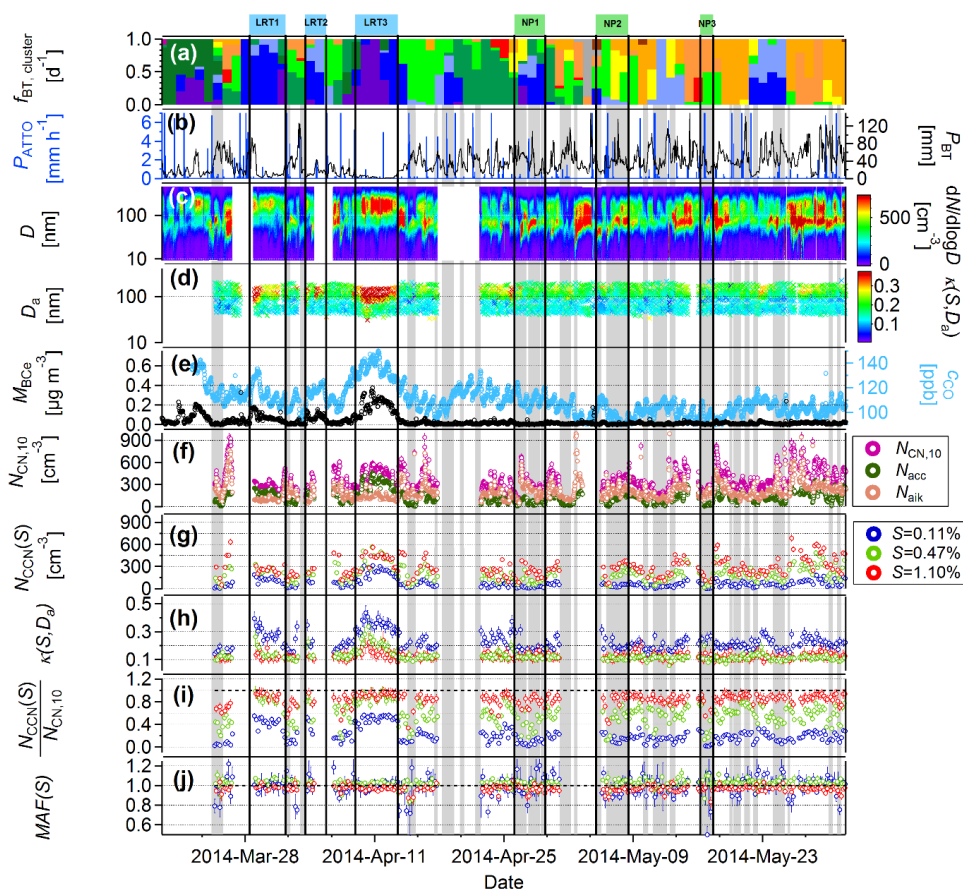
Figure 2. Overview plot illustrating selected meteorological, trace gas, aerosol, and CCN time series for representative wet season conditions in the central Amazon. Shown time period from 23 Mar until 31 May covers comparatively clean extended time frame throughout entire CCN measurement period. Individual panels represent: (a) Daily frequency of occurrence of 15 different BT clusters, $f_{BT,cluster}$, with color code corresponding to Fig. 1. (b) Precipitation rate P_{ATTO} measured locally at the ATTO site and cumulative precipitation from HYSPLIT trajectory analysis P_{BT} as measure for aerosol wet deposition. (c) SMPS-derived time series of number size distributions spanning nucleation, Aitken, and accumulation modes. (d) CCNC-derived time series of $\kappa(S,D_a)$ size distributions. (e) Concentrations of biomass burning tracers CO mole fraction, c_{CO}, and BC_e mass concentration, M_{BCe}. (f) Total number concentrations of entire aerosol population $N_{CN,10}$, Aitken mode particles N_{Ait}, and accumulation mode particles N_{acc}. (g) CCN concentrations $N_{CCN}(S)$ for selected supersaturations S. (h) Hygroscopicity parameter $\kappa(S,D_a)$ for selected S, (i) CCN efficiencies $N_{CCN}(S)/N_{CN,10}$ for selected S. (j) Maximum activated fraction $MAF(S)$ for selected S. All CCN data is provided in original time resolution of about 4.5 h. Grey vertical shadings represent near-pristine periods according to definition in Sect. 2.3. Vertical markers $NP1$, $NP2$, and $NP3$ represent case studies on selected near-pristine (NP) episodes for detailed analysis in Sect. 3.4. Vertical markers $LRT1$, $LRT2$, and $LRT3$ represent case studies on African LRT influence for detailed analysis in Sect. 3.5.
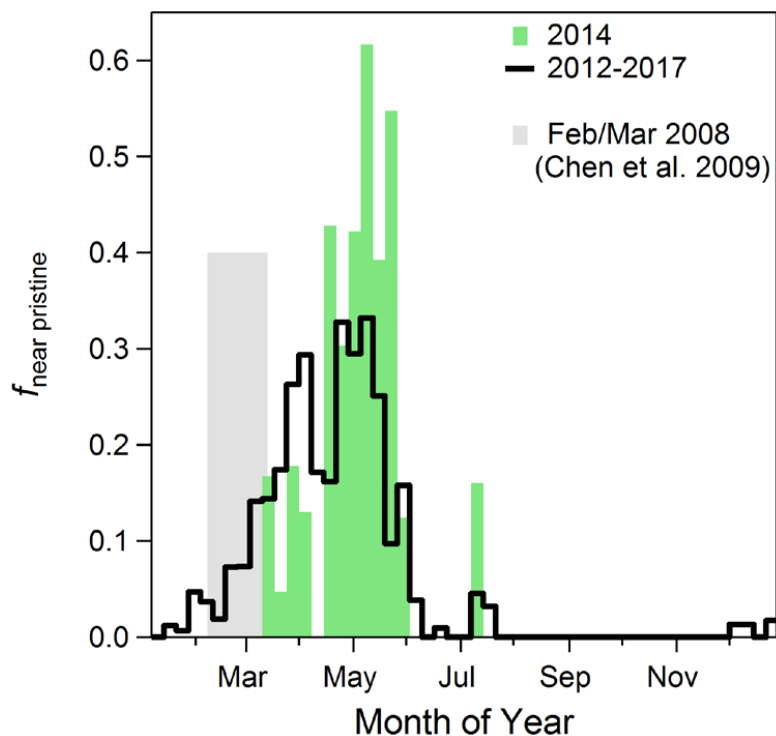
Figure 3. Seasonality of relative fraction of near-pristine days, $f_{\text{near pristine}}$, in the ATTO region. Near-pristine episodes were defined in Sect. 2.3. Data is shown as weekly averages for time period from Mar 2012 until May 2017 (black line) and for 2014 only (green shading). Data shows that year 2014, which comprises most of the present CCN data, had highest fraction of near-pristine days in second half of the wet season (i.e., Apr and May) in agreement with multi-year trend. For comparison, the relative fraction of periods with dominant in-Basin processes accordingly to Chen et al. (2009) – interpreted here as similar to near-pristine conditions – is shown as grey shading and agrees with our data.
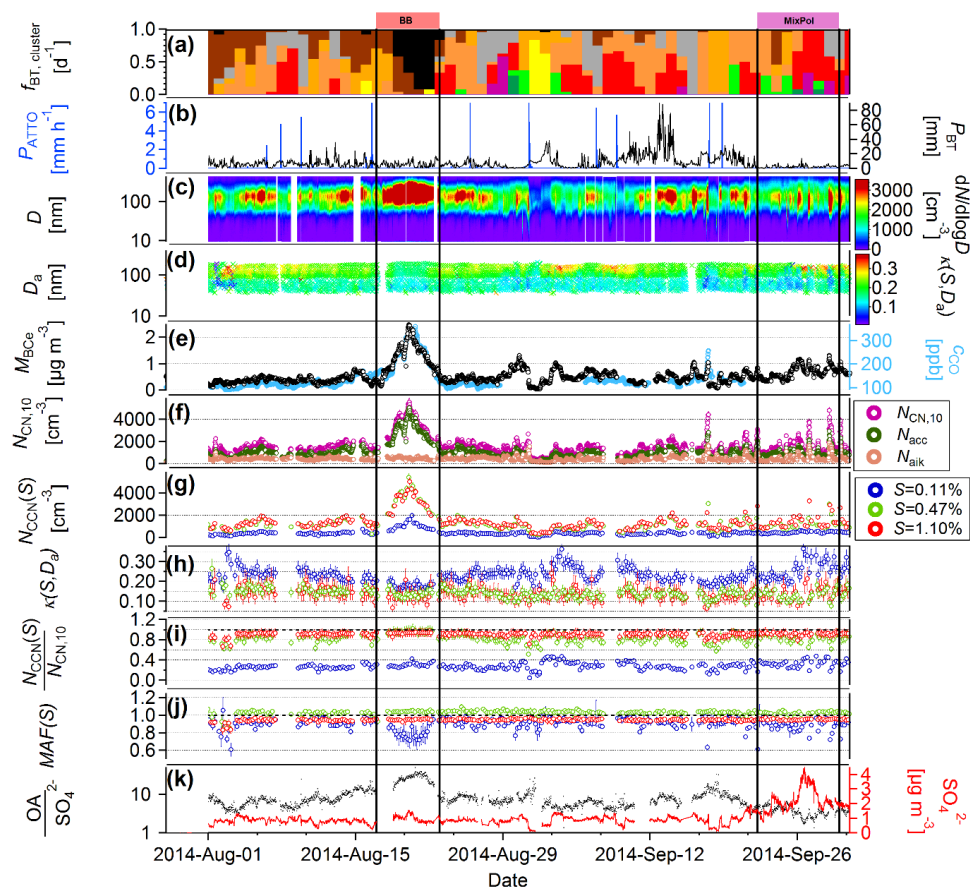
Figure 4. Overview plot illustrating selected meteorological, trace gas, aerosol, and CCN time series for representative dry season conditions in the central Amazon. Shown time period from 01 Aug until 31 Sep covers most polluted time frame throughout entire CCN measurement period. Individual panels represent: (a) Daily frequency of occurrence of 15 different BT clusters, $f_{BT,cluster}$, with color code corresponding to Fig. 1. (b) Precipitation rate P_{ATTO} measured locally at the ATTO site and cumulative precipitation from HYSPLIT trajectory analysis P_{BT} as measure for aerosol wet deposition. (c) SMPS-derived time series of number size distributions spanning nucleation, Aitken, and accumulation modes. (d) CCNC-derived time series of $\kappa(S,D_a)$ size distributions. (e) Concentrations of biomass burning tracers CO mole fraction, c_{CO}, and BC$_e$ mass concentration, M_{BCe}. (f) Total number concentrations of entire aerosol population $N_{CN,10}$, Aitken mode particles N_{Ait}, and accumulation mode particles N_{acc}. (g) CCN concentrations $N_{CCN}(S)$ for selected supersaturations S. (h) Hygroscopicity parameter $\kappa(S,D_a)$ for selected S, (i) CCN efficiencies $N_{CCN}(S)/N_{CN,10}$ for selected S. (j) Maximum activated fraction $MAF(S)$ for selected S. (k) ACSM-derived sulfate mass concentration, $m_{sulfate}$, and organic-to-sulfate ratio, OA/SO$_4^{2-}$. All CCN data is provided in original time resolution of about 4.5 h. Vertical marker *BB* represent case studies on biomass burning episodes for detailed analysis in Sect. 3.6. Vertical marker *MixPol* represent case studies on mixed pollution conditions for detailed analysis in Sect. 3.7.
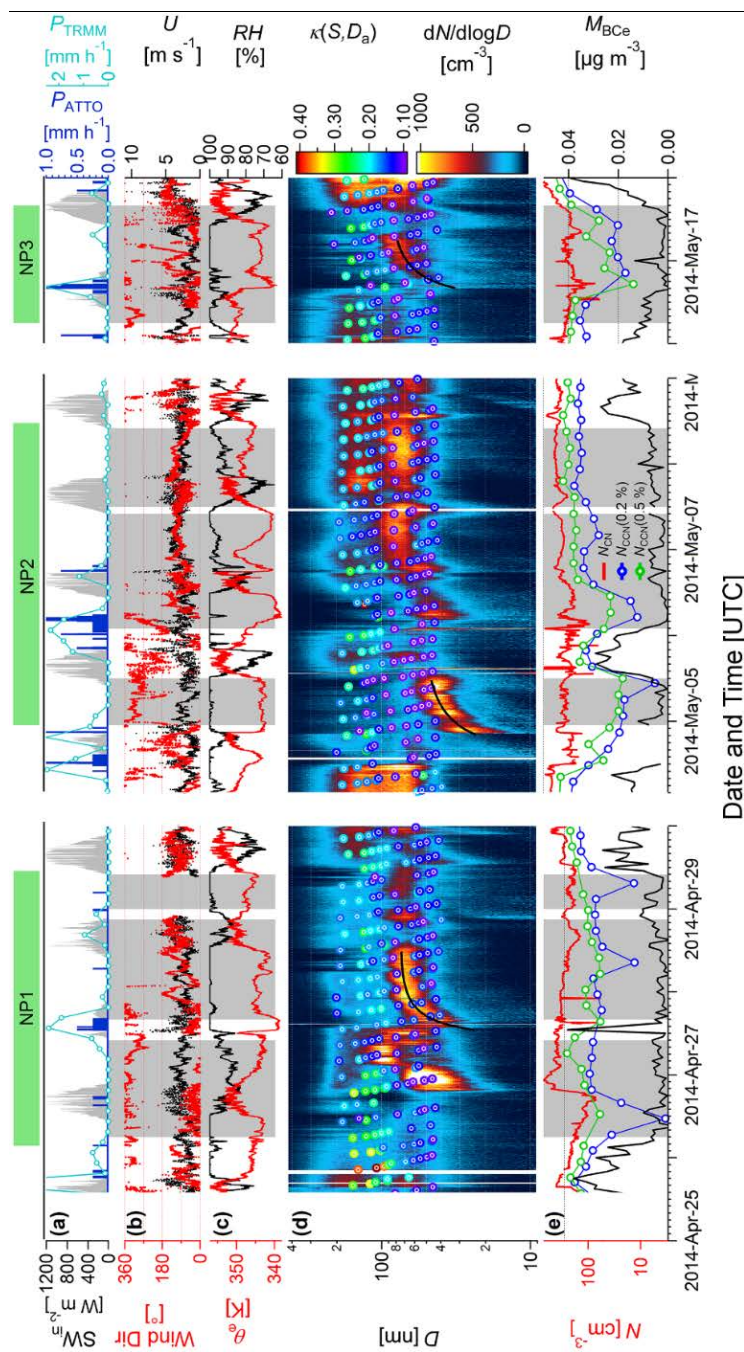
Figure 5. Selected meteorological, aerosol, and CCN time series from ground-based ATTO site measurements for near-pristine case study periods *NP1*, *NP2*, and *NP3* (see Fig. 3). (a) Precipitation rates from TRMM satellite mission, P_{TRMM}, and *in situ* measurements at the ATTO site, P_{ATTO}. (b) Wind direction and wind speed, U, at the ATTO site. (c) Equivalent potential temperature, θ_e, and relative humidity, RH, at the ATTO site. (d) Overlay of two data layers showing aerosol number size distribution contour plot (dN/dlogD) as well as color coded markers, representing time series of $\kappa(S,D_a)$ size distributions, and (e) CCN concentrations $N_{CCN}(S)$ for two selected S levels, total aerosol number concentration $N_{CN,10}$, and BC_e mass concentration M_{BCe}. Grey vertical shadings represent near-pristine periods according to definition in Sect. 2.3.

Figure 6. Overview of case studies conditions near-pristine (*NP*), long-range transport of African dust (*LRT*), biomass burning (*BB*), and mixed pollution of African and Amazonian sources (*MixPol*) showing: Size dependence of hygroscopicity parameter $\kappa(S,D_a)$, number size distributions of total aerosol particles $N_{CN}(D)$, and number size distributions of cloud condensation nuclei $N_{CCN}(S,D)$ at all 10 S levels (S = 0.11-1.10 %) (left column) and CCN efficiency spectra with erf fits (right column). For the size distributions (left): Values of $\kappa(S,D_a)$ for every S level are plotted against their corresponding midpoint activation diameter $D_a(S)$. For $\kappa(S,D_a)$, the error bars represent 1 std. For $D_a(S)$, the experimentally derived error is shown. The standard errors of the number size distributions – $N_{CN}(D)$ and $N_{CCN}(S,D)$ – are indicated as shading of the individual lines. For the CCN efficiency spectra (right): $N_{CN,10}$ was chosen as reference concentration. The experimental data was fitted with single- or double-erf fits (dashed lines with shading as uncertainty of the fits). The error bars at the markers represent the measurement error in S and 1 std in $N_{CCN}(S)/N_{CN,10}$ dimension. The shading represents the uncertainty of the fits. An overview of the erf fits from all case studies can be found in Fig. 10. The parameters of all erf fits are summarized in Table 2. Data for *NP* conditions, shown in (a) and (b), represent averages of *all* near-pristine episodes during the entire CCN measurements as defined in Sect. 2.3. For the *NP* CCN efficiency spectra, the double-erf fit is the better representation, although the single-erf fit also works as a good approximation. The CCN efficiency spectrum representing "green ocean" condition according to Roberts et al., (2001) agrees well with the NP data. Data for *LRT* conditions, shown in (c) and (d), represent the *LRT3* period as shown in Fig. 2. A single-erf fit describes the experimental data accurately. Data for *BB* conditions, shown in (c) and (d), represent time period in Aug 2014 as shown in Fig. 4. For the *BB* case, the experimental data has been fitted with a single-erf fit in two modifications: (i) The 'default' fit with predefined variables v_1 = 0.5 and a_1 = 0.5 as utilized for all other case studies tends to overestimate $N_{CCN}(S)/N_{CN,10}$ at high S. (ii) A corresponding fit with free variables v_1 and a_1 describes the experimental data more accurately. For comparison, CCN efficiency spectra representing rather fresh BB smoke according to Andreae et al., (2004) were added, which agree well with our data on aged BB smoke. Data for *MixPol* conditions, were separated into a *high κ* case (g), presenting sulfate-rich African aerosols and a *low κ* case (h), representing local fire plumes. *MixPol* CCN efficiency spectra are combined in (i) including single-erf fits.
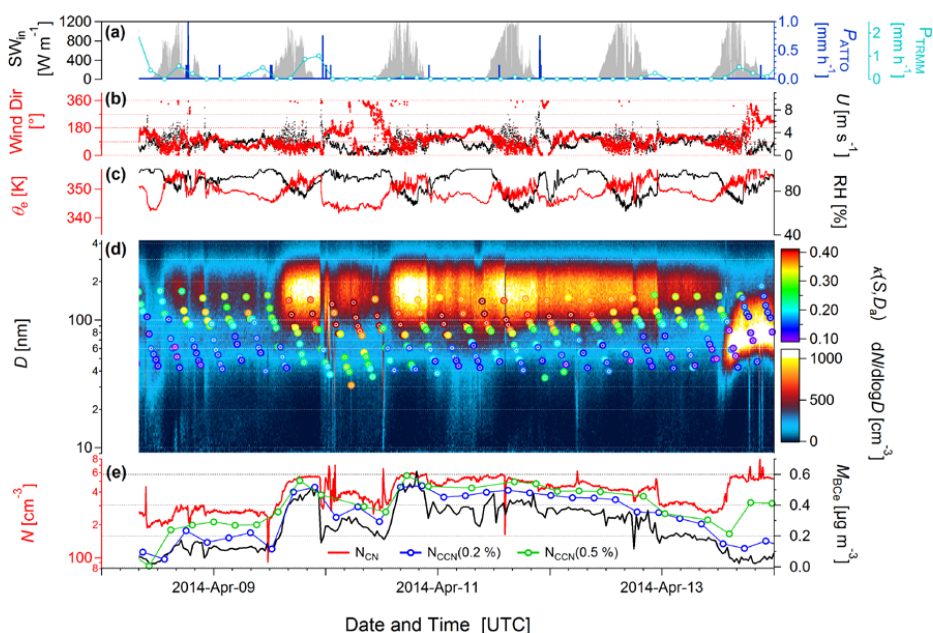
Figure 7. Selected meteorological, aerosol, and CCN time series from ground-based ATTO site measurements for long-range transport study period *LRT3* (see Fig. 3). (a) Precipitation rates from TRMM satellite mission, P_{TRMM}, and *in situ* measurements at the ATTO site, P_{ATTO}. (b) Wind direction and wind speed, U, at the ATTO site. (c) Equivalent potential temperature, θ_e, and relative humidity, RH, at the ATTO site, (d) Overlay of two data layers showing aerosol number size distribution contour plot (dN/dlog$D$) as well as color coded markers, representing time series of $\kappa(S,D_a)$ size distributions, and (e) CCN concentrations $N_{CCN}(S)$ for two selected S levels, total aerosol number concentration $N_{CN,10}$, and BC$_e$ mass concentration M_{BCe}.
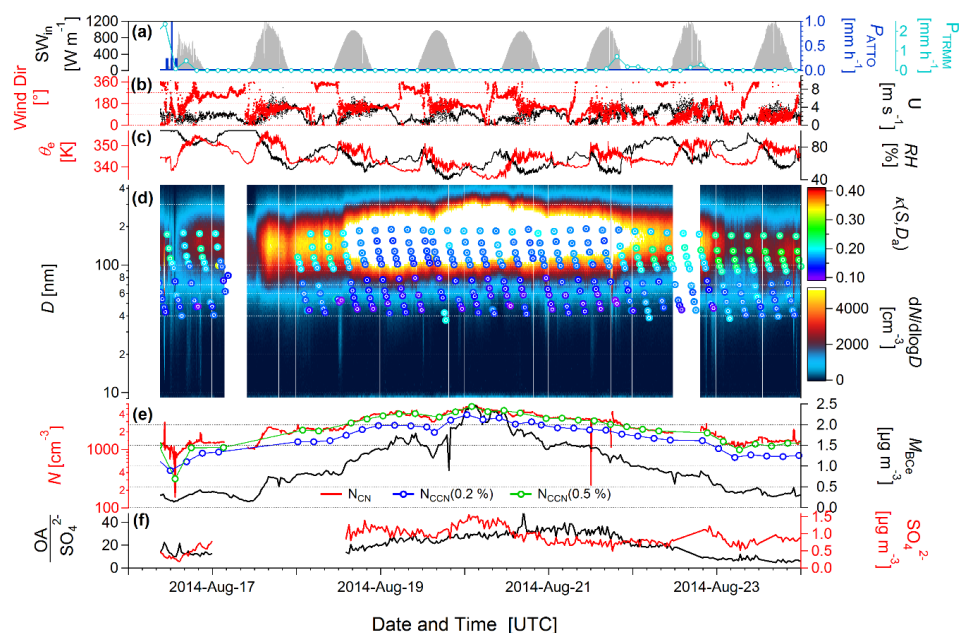
Figure 8. Selected meteorological, aerosol, and CCN time series from ground-based ATTO site measurements for biomass burning case study period _BB_ (see Fig. 5). (a) Precipitation rates from TRMM satellite mission, P_{TRMM}, and _in situ_ measurements at the ATTO site, P_{ATTO}. (b) Wind direction and wind speed, U, at the ATTO site. (c) Equivalent potential temperature, θ_e, and relative humidity, RH, at the ATTO site, (d) Overlay of two data layers showing aerosol number size distribution contour plot (dN/dlog$D$) as well as color coded markers, representing time series of $\kappa(S,D_a)$ size distributions, and (e) CCN concentrations $N_{CCN}(S)$ for two selected S levels, total aerosol number concentration $N_{CN,10}$, and BC_e mass concentration M_{BCe}. (f) ACSM-derived sulfate mass concentrations and organic-to-sulfate mass ratio.

Figure 9. Selected meteorological, aerosol, and CCN time series from ground-based ATTO site measurements for mixed pollution case study period *MixPol* (see Fig. 5). (a) Precipitation rates from TRMM satellite mission, P_{TRMM}, and *in situ* measurements at the ATTO site, P_{ATTO}. (b) Wind direction and wind speed, U, at the ATTO site. (c) Equivalent potential temperature, θ_e, and relative humidity, RH, at the ATTO site, (d) Overlay of two data layers showing aerosol number size distribution contour plot (dN/dlog$D$) as well as color coded markers, representing time series of $\kappa(S,D_a)$ size distributions, and (e) CCN concentrations $N_{CCN}(S)$ for two selected S levels, total aerosol number concentration $N_{CN,10}$, and BC$_e$ mass concentration M_{BCe}. (f) ACSM-derived sulfate mass concentrations and organic-to-sulfate mass ratio. The vertical shading highlights episodes under the influence of local/regional fires (red) vs. periods that are dominated by background pollution (grey).
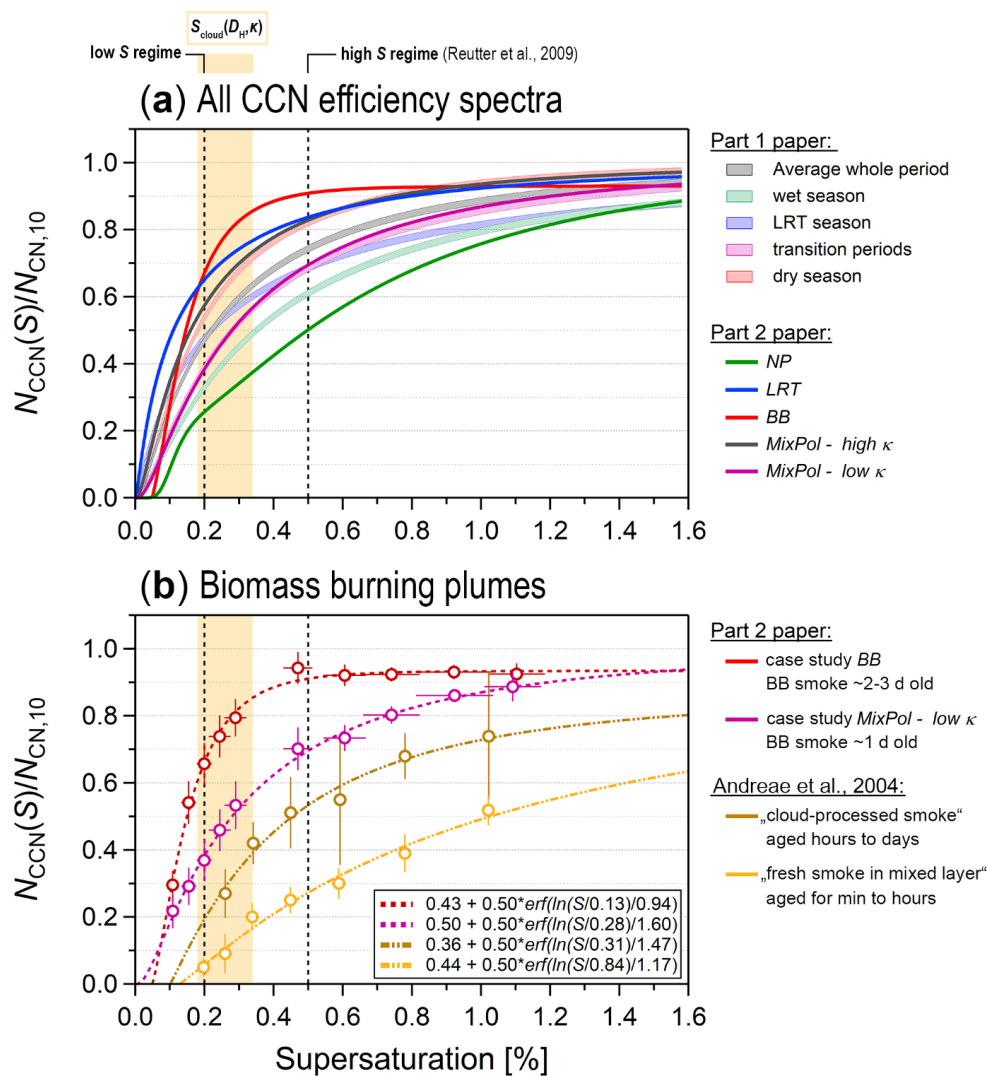
Figure 10. Concluding comparison of CCN efficiency spectra. **(a)** Combination of all case study spectra from present part 2 paper and seasonally averaged spectra from companion part 1 study (M. Pöhlker et al., 2016). **(b)** Combination of CCN efficiency spectra for biomass burning plumes in different states of atmospheric aging. Spectra originate from *BB* and *MixPol/low* κ case studies in present work as well as from previous study by Andreae et al. (2004). Vertical markers represent low *S* and high *S* regimes according to Reutter et al. (2009) (dashed lines) as well as estimated peak supersaturations at cloud base, $S_{cloud}(D_H,\kappa)$ in the ATTO region according to Krüger et al., (2014) (orange shading).